

Atomically precise surface chemistry of zirconium and hafnium metal oxo clusters beyond carboxylate ligands

Ajmal Roshan Unniram Parambil,^{†,‡,¶} Rohan Pokratath,[‡] Muhammed Jibin Parammal,[‡] Evert Dhaene,[‡] Dietger Van den Eynden,^{‡,§} Sandor Balog,^{||} Alessandro Prescimone,[‡] Ivan Infante,[⊥] Patrick Shahgaldian,[†] and Jonathan De Roo^{*,‡}

[†]*Institute of Chemistry and Bioanalytics, School of Life Sciences, University of Applied Sciences and Arts Northwestern Switzerland, 4132 Muttenz, Switzerland*

[‡]*Department of Chemistry, University of Basel, Mattenstrasse 22, 4058 Basel, Switzerland*

[¶]*Swiss Nanoscience Institute, Klingelbergstrasse 82, 4056 Basel*

[§]*Department of Chemistry, University of Ghent, Krijgslaan 281, 9000 Ghent, Belgium*

^{||}*Adolphe Merkle Institute, University of Fribourg, 1700 Fribourg, Switzerland*

[⊥]*BCMaterials, Spain*

E-mail: jonathan.deroo@unibas.ch

Abstract

The effectiveness of nanocrystals in many applications greatly depends on their surface chemistry. Here, we leverage the atomically precise nature of zirconium and hafnium oxo clusters to gain fundamental insight into the thermodynamics of ligand binding. Through a combination of theoretical calculations and experimental spectroscopic techniques, we determine the multifaceted interaction between the $M_6O_8^{8+}$

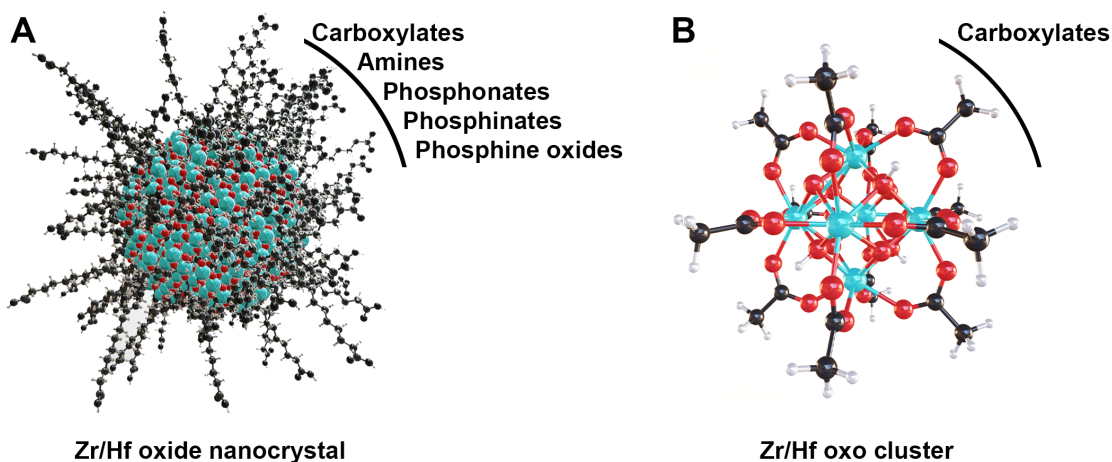
(M = Zr, Hf) cluster surface and various ligands: carboxylates, phosphonates, dialkylphosphinates, and monosubstituted phosphinates. We refute the common assumption that the adsorption energy of an adsorbate remains unaffected by the surrounding adsorbates. We find that dialkylphosphinic acids are too sterically hindered to yield complete ligand exchange, even though a single dialkylphosphinate has similar binding affinity to a phosphonate. On the other hand, monoalkyl or monoaryl phosphinic acids replace carboxylates quantitatively and we obtained the crystal structure of $M_6O_8H_4(O_2P(H)Ph)_{12}$ (M = Zr, Hf), giving a unique insight into the exact binding mode of monoalkylphosphinate. Finally, phosphonic acids cause a partial structural reorganization of the metal oxo cluster into amorphous metal phosphonate as indicated by pair distribution function analysis. These results rationalize the absence of phosphonate-capped M_6O_8 clusters and the challenge in preparing Zr phosphonate metal-organic frameworks. We further reinforce the notion that monoalkylphosphinates are carboxylate mimics with superior binding affinity.

Introduction

Group 4 metal oxo clusters are the building blocks of metal-organic frameworks (MOFs),¹⁻⁵ while the discrete clusters are used in polymer composites,⁶⁻⁸ and as catalysts.⁹⁻¹³ Conceptually, discrete oxo clusters are close to metal oxide nanocrystals, see **Scheme 1**. Both have an inorganic core capped with an organic ligand shell, mostly carboxylates.^{14,15} One can regard the prototypical $Zr_6O_8H_4(OOCR)_{12}$ (**Zr6**) cluster as the smallest possible nanoparticle, with the additional advantage that the cluster is atomically precise while nanocrystals are inherently polydisperse.

Zr6 clusters feature six zirconium atoms arranged in an octahedron and eight μ_3 -oxygen atoms, one on every facet of the octahedron. Half of these μ_3 -oxygens is protonated.^{16,17} The cationic core is coordinated by twelve carboxylate ligands. While **Zr6** is most common, there are zirconium clusters with a nuclearity of 3-10, 12, 18, 26 or 36 depending on the organic

ligands and reaction conditions.^{14,18,19} Short-chain carboxylates are most used in nonaqueous synthesis.^{14,19} Interestingly, **Zr6** clusters dimerize to **Zr12** clusters through four intercluster bridging ligands if the ligands provide little sterical hindrance.^{12,14} In such **Zr12** clusters, there are 4 distinct types of ligand environments: chelating, belt bridging, intercluster bridging and inner-face bridging.¹⁷ Hafnium has very similar reactivity to zirconium and forms the same types of clusters, following the same rules on dimerization.^{12,14} The octahedral oxo cluster motif is also found for other tetravalent metals such as cerium and thorium.^{20–23} Titanium is an exception in the tetravalent series due to its reluctance to support a coordination number of eight. It rather forms $\text{Ti}_8\text{O}_8(\text{OOCR})_{18}$,²⁴ or $\text{Ti}_6\text{O}_6(\text{OR})_6(\text{OOCR})_6$ clusters.²⁵



Scheme 1: (A) Schematic representation of a colloidally stable zirconium/hafnium oxide nanocrystal depicting the inorganic core and organic ligand shell. (B) The structure of $\text{M}_6\text{O}_8\text{H}_4(\text{OOCR})_{12}$, where the M_6O_8 core is capped with twelve ligands, $\text{M}=\text{Zr}/\text{Hf}$. The ligands that have been reported to cap nanocrystals and clusters in nonpolar media are listed. Cyan atoms represent zirconium or hafnium, all other atoms follow conventional CPK coloring.

Colloidal nanocrystals constitute a broad materials class ranging from metal colloids,^{26–29} over quantum dots,^{30,31} to metal oxide nanocrystals.^{14,32} Their uses are equally broad from optoelectronic devices to biomedical applications.^{33–36} In each of these applications the surface plays a crucial role, making nanocrystal surface chemistry an important field of research. Ligands can be either inorganic or organic,^{37,38} with the latter being mostly used in nanocrystal synthesis.^{39,40} The surface of oxide nanocrystals is highly similar to that of oxo clusters.

The ability of the surface oxygen atoms to bind protons in nonpolar solvents was also demonstrated for oxide nanocrystals,^{41,42} while this was established in polar solvents. On the other hand, anions or neutral Lewis bases coordinate to the metal sites of nanocrystal surfaces, and their binding is usually confirmed through NMR spectroscopy.^{38,43,44} Focusing on nonpolar solvents and zirconium/hafnium oxides, the ligand binding affinity can be roughly ranked as phosphonic acids ($\text{RPO}(\text{OH})_2$) \approx monoalkylphosphinic acids ($\text{R}(\text{H})\text{PO}(\text{OH})$) \gg carboxylic acids (RCOOH).^{45,46} Neutral Lewis bases such as amines, alcohols, and phosphine oxides typically bind much weaker.^{42,47,48} In addition to the binding group, also sterics play a role, with sterically hindered ligands binding weakly or only at facet edges.^{49,50} Finally, nanocrystal surfaces have many different binding sites, each with their own equilibrium binding constant, rendering thermodynamic analyses highly complex.^{51,52}

In this context, the atomically precise nature of oxo clusters is appealing for surface chemistry studies.⁵³ Focusing on nonpolar solvents and zirconium/hafnium oxo clusters, only carboxylate ligands were explored.¹⁵ Carboxylate-for-carboxylate exchange was studied. It was shown that at room temperature, there is no interconversion between **Zr6** and **Zr12**, while at elevated temperatures the ligand becomes structure-directing.^{12,54} The absence of any reports on ligand exchanges with phosphinic or phosphonic acids is striking. By direct synthesis from zirconium alkoxide and phosphonic acids, various oxoalkoxy clusters are formed instead of the Zr_6O_8 unit.^{55,56} Only from ZrCl_4 and dimethylphosphate ligands in dimethylformamide, a Zr_6O_8 cluster was prepared.⁵⁷ Also in the case of titanium only various oxoalkoxy species are produced by reacting titanium alkoxides with phosphonic or diphenylphosphinic acid.⁵⁸⁻⁶¹ Ce_6O_8 clusters were formed with mixed ligand shells consisting of eight pivalate and four diphenylphosphinate ligands.⁶² Overall, phosphor-based ligands are poorly explored in the oxo cluster field and no spectroscopic or thermodynamic studies have been reported. A Zr MOF with M_6O_8 as secondary building unit and phosphonate linkers was only synthesized from their parent carboxylate MOF by solvent assisted linker exchange for a phosphinate ligand and subsequent oxidation to phosphonate.⁶³

Here, we study the surface chemistry of Zr_6O_8 and Hf_6O_8 oxo clusters through ligand exchange reactions, both experimentally and computationally. Choosing carboxylate-capped **Zr12** and **Zr6** clusters as starting points, we modify their surface with a variety of phosphonate and mono/di-substituted phosphinate ligands in chloroform. The extent of exchange is monitored through solution ^1H NMR, ^{31}P NMR, and FTIR spectroscopy. The structural integrity of the core is assessed by X-ray total scattering and Pair Distribution Function analysis. We find that a single exchange of a carboxylate for a phosphonate or phosphinate is thermodynamically favorable. However, full exchange of all 12 carboxylates per Zr_6O_8 core is sterically impeded for di-substituted phosphinic acids. Monoalkyl- or monoarylphosphinic acids quantitatively exchange all carboxylates while phosphonates cause disintegration of the Zr_6O_8 core and form zirconium phosphonate gels. In case of monophenylphosphinate-capped **Zr6** clusters, single crystal diffraction revealed the all-bridging binding mode of the ligand.

Results

In silico ligand exchange

We first evaluate ligand exchanges *in silico* by performing a set of density functional theory (DFT) calculations. We choose the crystal structure of $\text{Zr}_6\text{O}_8\text{H}_4(\text{OOCMe})_{12}$ (**Zr6**-acetate) as the starting model due to its simplicity, featuring twelve identical bridging acetate ligands (**Figure S1**).⁶⁴ The structure is an exception to the dimerization rule owing to its crystallization from an aqueous solution.¹⁴ We exchange the twelve acetate ligands in twelve steps, each time placing the new ligands on the cluster as far away as possible from each other to minimize interactions (**Figure S3 - S8**). As incoming ligand, we explore ethyl and methylphosphonic acid, monoethyl and monomethylphosphinic acid, and diethyl and dimethylphosphinic acid (**Figure 1**). The geometry of all structures are optimized at DFT/PBE/DZVP level of theory (more computational details in the experimental section) and the ΔH for the exchanges are plotted in **Figure 1B**. All optimized structures are available as xyz-files in the Support-

ing information. The same calculations were performed for hafnium oxo clusters and the results are identical (**Figure S2**).

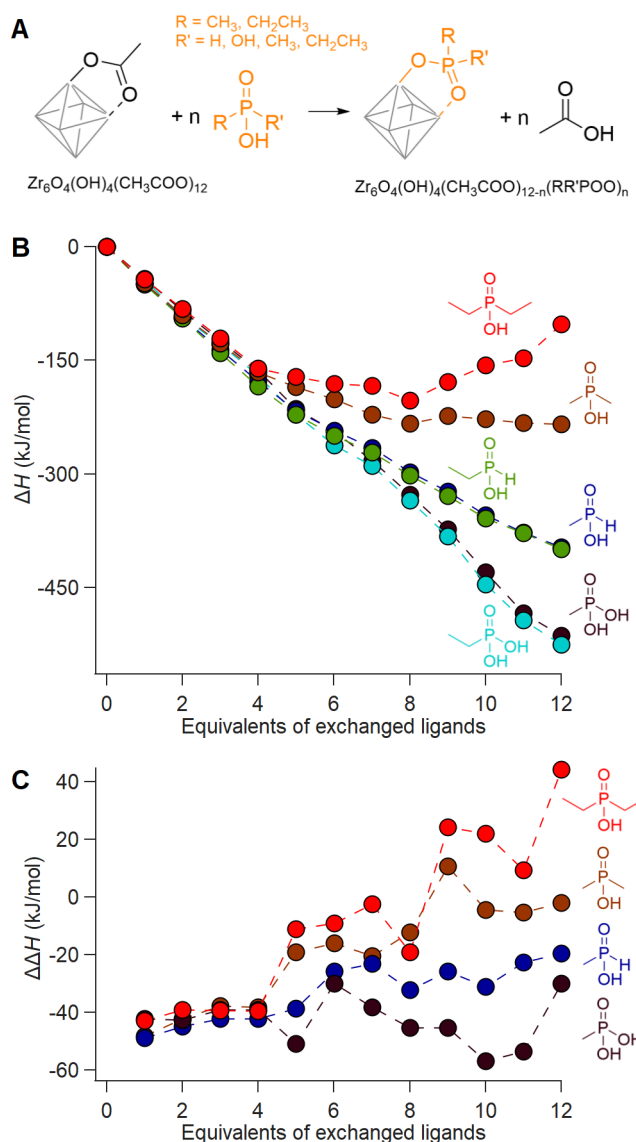


Figure 1: (A) Scheme representing the exchange of acetate ligands for phosphor-based ligands on a fully bridged **Zr6** cluster. (B) Enthalpy of ligand exchange reactions as a function of equivalents of exchanged ligands, ΔH . (C) The enthalpy change for every step, $\Delta\Delta H$.

Phosphonic acids present a clear downhill path from the first to the last exchange and have an average; $\Delta H = -43$ kJ per mole of exchanged ligand. Monoalkylphosphonic acids behave similarly but have a slightly lower average; $\Delta H = -33$ kJ per mole of exchanged ligand. The difference between the average values for phosphonic and monoalkylphosphonic acids

(10 kJ/mol) is slightly larger than the experimentally determined free energy of exchange on hafnium oxide nanocrystals; $\Delta G = 2$ kJ/mol in favor of phosphonic acids.⁴⁶ Apart from entropic contributions, the lower energy of phosphonate-capped clusters can be attributed to the regular pattern of hydrogen bonds on the cluster (see **Figure S7** and **S8**). Interestingly, there is little difference between the ethyl and methyl variants for both monoalkylphosphinic and phosphonic acids, giving confidence that longer chains will have little additional steric impact. For dimethylphosphinic acid, the average exchange enthalpy is $\Delta H = -20$ kJ per mole of exchanged ligand. However, this lower value masks the fact that for the first four exchanges, the ΔH for each step (i.e., $\Delta\Delta H$) is about the same as for monoalkylphosphinic acids (see **Figure 1C**). From the fifth exchange, $\Delta\Delta H$ becomes less negative and there is hardly any driving force for the last four exchanges. The effect is exacerbated for diethylphosphinic acid. The first four exchanges are highly exothermic, the second four are slightly exothermic and the final four are even endothermic. The discontinuities at the fifth exchange and the ninth exchange are a consequence of our ligand positioning strategy. The first four exchanges happen on the edges of the equatorial plane of the **Zr6** octahedron (**Figure S3**). The fifth incoming ligand cannot avoid interaction with the previously exchanged ligands. We thus predict that, experimentally, dialkylphosphinic acids will feature a mixed ligand shell with carboxylates. There is a clear thermodynamic minimum which lies at 8 exchanged ligands for diethylphosphinic acid. For other disubstituted phosphinic acids, its precise location will depend on the steric bulk of the substituents. This is in line with the literature reports on **Ce6** oxo clusters with mixed ligand shells of pivalate and diphenylphosphinate.⁶² Comparing **Zr6** clusters with nanocrystals, clusters have the maximum surface curvature. Any particle larger than **Zr6** has even less space to accommodate sterically hindered ligands.

Our theoretical approach clearly outlines that one common assumption in surface chemistry is here invalid: that the adsorption energy of an adsorbate is independent of the surrounding adsorbates. This assumption is key in the Langmuir model but we clearly show

here that not every binding site is equal. Interestingly, every binding site is equivalent until the first ligand exchange happens. This is thus different from the previously observed binding site heterogeneity on CdSe,⁵¹ but rather agrees with composition-dependent thermodynamics.⁵² To assess the intrinsic binding affinity of different ligands, we thus compare the enthalpy change for the first exchanges only. Surprisingly, all studied ligands have about the same $\Delta\Delta H$ for the first four exchanges; averaging -41 kJ/mol except for monomethylphosphinic acid which averages -44 kJ/mol, thus slightly more exothermic. It is striking that monoalkylphosphinic acids are stronger binders than phosphonic acids. This is probably because there are not yet hydrogen bonds established necessary for a cooperative effect in the case of phosphonates (observed in **Figure 1C** between 6 and 11 equivalents).

The **Zr6** core structure undergoes expansion during phosphinate/phosphonate ligand exchanges, a trend visualized by plotting all the *cis* and *trans* Zr-Zr distances within an oxo cluster core, see **Figure 2**. When a first (bridging) acetate is exchanged with a (bridging) monomethylphosphinate, there is a clear outlier in the *cis* Zr-Zr distances, representing one longer distance of 3.6 Å. This data point is assigned to the Zr-Zr pair that is bridged by the phosphinate. The second exchange yields another long *cis* Zr-Zr distance, and there is asymmetry in the *trans* Zr-Zr distances with two longer distances and one shorter distance compared to the starting position. On average, both *cis* and *trans* distances are increasing with progressing ligand exchange. While the final structure is highly symmetric, the structures with mixed ligand shells are highly distorted and we find the analysis in **Figure 2** useful to objectively assess the structure and its symmetry. The analysis is made convenient through a python script that extracts all the distances, see experimental section for more details. The above trend is consistent across all studied ligands (**Figure S9-S12**). We conclude that phosphinate and phosphonate ligands exert expansive strain onto the oxo clusters.

When synthesized from nonaqueous solvents, the acetate ligands stabilize a **Zr12** cluster, the dimer of two **Zr6** clusters.^{5,16,17} This makes the ligand shell highly complex with multiple

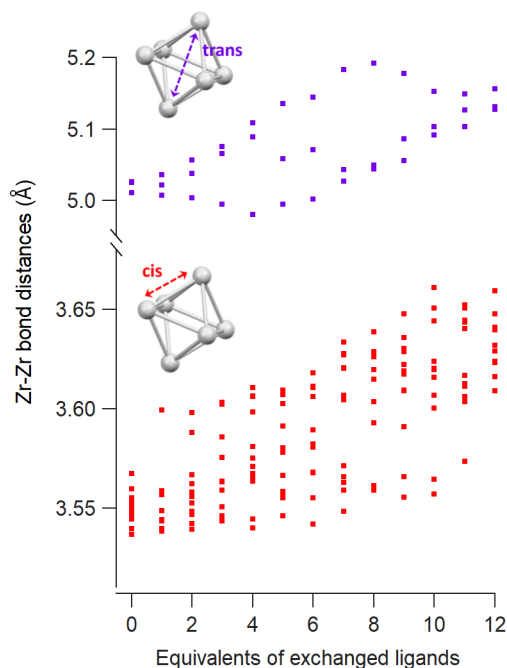


Figure 2: *cis* and *trans* Zr-Zr distances as a function of the equivalents of exchanged methylphosphinate ligands obtained from DFT calculations.

binding sites (**Figure 3A**). To explore this complexity, we exchanged one acetate ligand at different positions for phosphinate and phosphonate ligands (**Figure 3B** and **S13**). All exchanges are exothermic but the extent depends on the binding site and the incoming ligand. The belt-bridging position provides generally the most favorable exchange whereas the inner face-bridging position clearly shows a smaller ΔH for the sterically hindered dimethylphosphinic acid. The intercluster-bridging position shows the largest variation being less exothermic for dimethylphosphinic acid and very exothermic for methylphosphonic acid. The latter makes hydrogen bonds with a remaining acetate ligand through the second acidic group, stabilizing the product. Exchanging a chelating acetate with a chelating phosphinate or phosphonate is the least exothermic. One can understand this through analysis of bond distances and bond angles. The chelating binding mode compresses the O-C-O bond angle of acetate from 122° (in free acetic acid) to 118° , yielding a strain of 3.3%. For methylphosphinate, the O-P-O bond angle is compressed from 116° to 106° , yielding a strain of 8.6%. The P-O bond distance is generally larger than the C-O bond distance due to the larger size

of the phosphorus atom. This places the two oxygen atoms farther apart from one another in phosphinate than in carboxylate. To obtain the best coordination environment zirconium pulls the oxygen atoms together and achieves a distance of 2.20 Å for acetate and 2.45 Å for methylphosphinate. Furthermore, the Zr-O bond distance is shorter (i.e., stronger) for chelating acetate (2.32 Å) compared to chelating methylphosphinate (2.37 Å). Hence the phosphinate ligand is more strained and Zr achieves a less favorable coordination environment, thus destabilizing the chelating mode for phosphinates. In contrast, in bridging acetate the O-C-O angle expands from 122° to 126°, whereas the O-P-O bond angle experiences no strain from free (116°) to bound (116°) phosphinate. The Zr-O bond length is the same for bridging carboxylate and phosphinate (2.20 Å), which is stronger than the chelating mode.

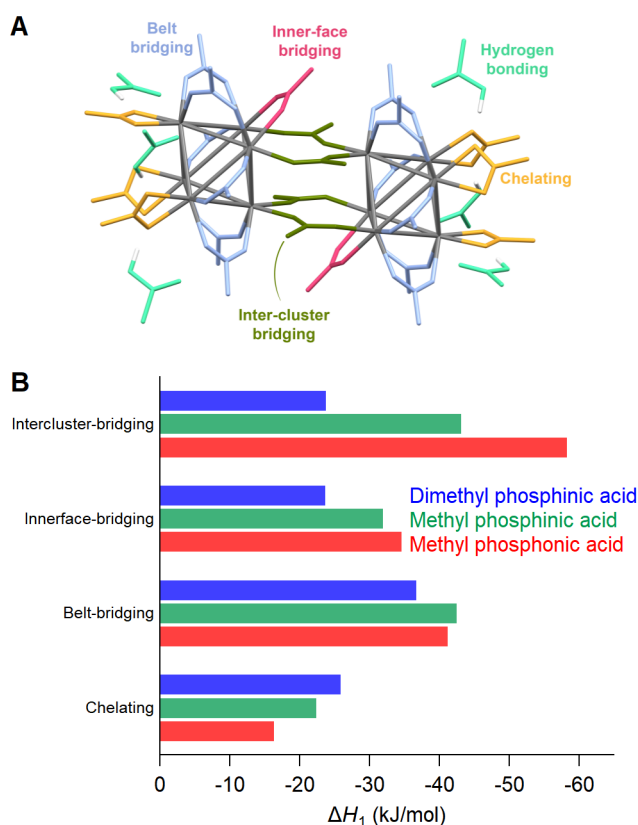


Figure 3: (A) Different binding modes of acetate ligands in the structure of $\text{Zr}_{12}\text{O}_{16}\text{H}_8(\text{OOCMe})_{24} \cdot 6 \text{MeCOOH}$ - CCDC-604528.^{5,17,54} (B) Enthalpy of ligand exchange reactions at different binding sites

Finally, we studied cluster dimerization by computing ΔH for the dimerization reaction.

We find that the conversion of **Zr6**-acetate to **Zr12**-acetate is exothermic (**Figure S14**). However, the conversion of **Zr6**-methylphosphinate to **Zr12**-methylphosphinate is highly endothermic, particularly when the phosphinate ligands keep the original binding mode of the carboxylates. When the binding mode of the phosphinates is relaxed to the bridging configuration, the dimerization becomes less endothermic but is still unfavorable. We conclude that the calculation predicts a preference for the monomer upon exchanging carboxylate ligands for phosphinates.

Ligand exchange for dialkylphosphinic acid

We now seek to confirm our computational results with experimental data and we first turn our attention to disubstituted phosphinic acids. As cluster model systems, we choose **Zr12**-acetate and **Zr6**-methylbutanoate, which were synthesized according to our earlier report.¹² We titrate the clusters with dioctylphosphinic acid and express the latter's quantity as equivalents relative to a $\text{Zr}_6\text{O}_8\text{H}_4^{12+}$ octahedron (**Figure 4**). There are twelve carboxylate ligands per $\text{Zr}_6\text{O}_8\text{H}_4^{12+}$ unit, both for the **Zr6** and the **Zr12** cluster. Upon addition of dioctylphosphinic acid to **Zr12**-acetate, one can discern six different resonances between 51 and 55 ppm in the ^{31}P NMR spectrum (**Figure 4A**). The different resonances are assigned to bound phosphinate and are a reflection of the binding site complexity on **Zr12** clusters (*vide supra*). In contrast, the addition of one equivalent dioctylphosphinic acid to **Zr6**-methylbutanoate results in one predominant resonance at 53 ppm (**Figure 4B**), indicating that the majority of bound phosphinate has the same environment. This is to be expected for the highly symmetrical **Zr6** cluster. The resonance for free dioctylphosphinic acid is absent in both cases, indicating a quantitative replacement of acetate, in line with the predictions by DFT.

Upon the addition of three equivalents dioctylphosphinic acid to **Zr12**-acetate, the most downfield resonance (at 55 ppm) disappears (**Figure 4A**). The same result is found in the titration with diethylphosphinic acid (**Figure S15**) and from the ^1H NMR spectrum (**Figure**

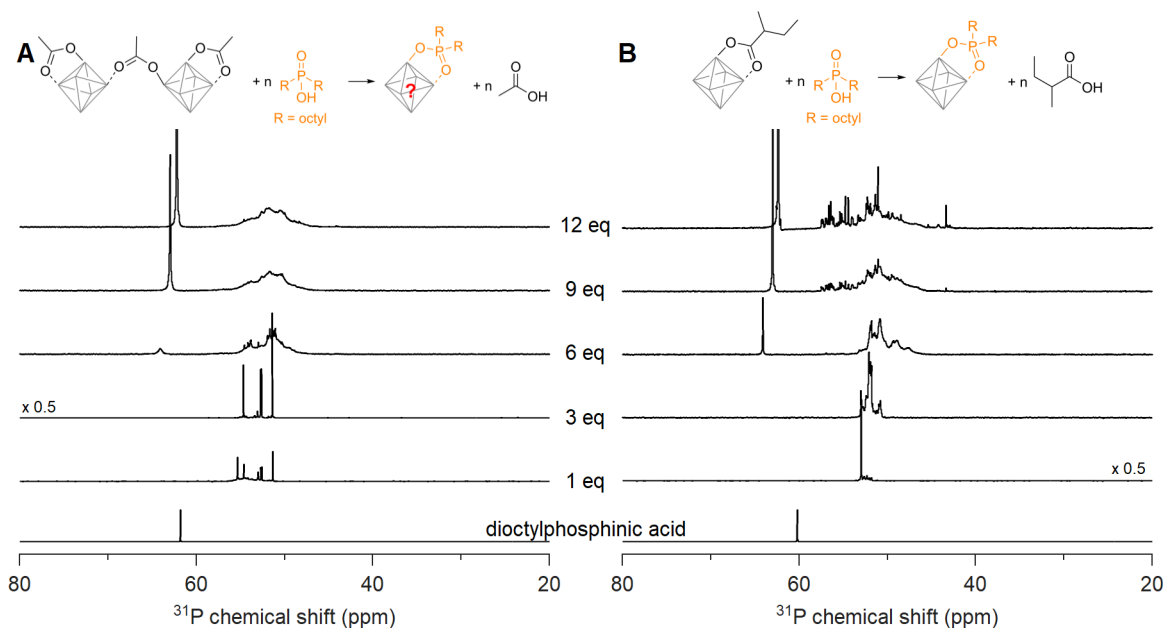


Figure 4: ^{31}P NMR spectra of the titrations of (A) **Zr12**-acetate and (B) **Zr6**-methylbutanoate with dioctylphosphinic acid (expressed as equivalents with respect to a monomer unit). The cluster concentration is 20 mg/mL in CDCl_3 . The reference ^{31}P NMR spectrum of dioctylphosphinic acid with one equivalent acetic acid is also provided.

S16B), we notice the disappearance of the characteristic pattern for **Zr12**-acetate. We infer that the cluster undergoes a structural reorganization, possibly into a **Zr6** structure. For six equivalents of dioctylphosphinic acid, we observe the resonance of free phosphonic acid, which further increases in intensity for 9 and 12 equivalents (**Figure 4A**). The same trend is observed for diethylphosphinic acid (**Figure S15B**), although the signal of free diethylphosphinic acid is less intense and appears only after 9 equivalents. This demonstrates that the composition of the mixed ligand shell depends on steric hindrance. For example, at 9 equivalents added, we integrate the free and bound resonances and derive that 7 dioctylphosphinates are bound, while 8.5 diethylphosphinates are bound. At 12 equivalents added, this becomes 7.4 bound dioctylphosphinates and 10 bound diethylphosphinates. Similar results are obtained for the **Zr6**-methylbutanoate clusters, titrated with dioctylphosphinic acid. For example, we determine 7.2 bound phosphinates at 9 equivalents added. For dioctylphosphinic acid, it is clearly hard to bind more than 8 equivalents and this threshold is remarkably close

to the thermodynamic minimum predicted by DFT, see **Figure 1B**. Note that the resonance of free phosphinic acid is shifting slightly during the titration, which is due its sensitivity to the acetic acid concentration (**Figure S26**).

Ligand exchange for aryl or alkyl phosphinic acids

We confirmed that the sterically hindered dialkylphosphinic acids cannot exchange all twelve acetate ligands per **Zr6**. Now we turn to a less sterically hindered analogue: monosubstituted phosphinic acids. We recently introduced them in nanocrystal synthesis,⁶⁵ and showed that their binding affinity for nanocrystal surfaces is comparable with that of phosphonic acids.⁴⁶ Here we titrate **Zr12**-acetate with phenyl- or hexylphosphinic acid (**Figure 5**). Note that the ³¹P NMR spectrum has a shifted range compared to **Figure 4** due to the different chemical shift of monosubstituted phosphinic acids, but the spectral width is the same in both graphs, so one can compare the peak widths visually. Upon titrating **Zr12**-acetate with hexylphosphinic acid, the first equivalent leads to multiple resonances, indicating a multitude of binding sites, similar to the titration with dioctylphosphinic acid. In contrast to dioctylphosphinic acid, we do not observe free hexylphosphinic acid at any point, indicating an irreversible and complete exchange. At 12 equivalents, the resonance of bound hexylphosphinate is more narrow (fwhm = 1.8 ppm, 372 Hz), compared to the resonance of bound dioctylphosphinate (fwhm = 3.2 ppm, 645 Hz), indicating a more homogeneous chemical environment for hexylphosphinate. The spectrum with 15 equivalents added shows a broad but discernible resonance for free hexylphosphinic acid (**Figure S28**).

A similar conclusion is reached for the titration with phenylphosphinic acid (**Figure 5B**). At 12 equivalents, the resonance of bound phenylphosphinate is even narrower (fwhm = 0.5 ppm), indicating a highly symmetric cluster structure. Similar to hexylphosphinic acid, the spectrum with 15 equivalents added shows a broad resonance for free phenylphosphinic acid (**Figure S27**). For both hexyl and phenylphosphinic acid, the ¹H NMR spectra (**Figure S17**) show the disappearance of the bound acetate resonances and only a singlet at ~ 2

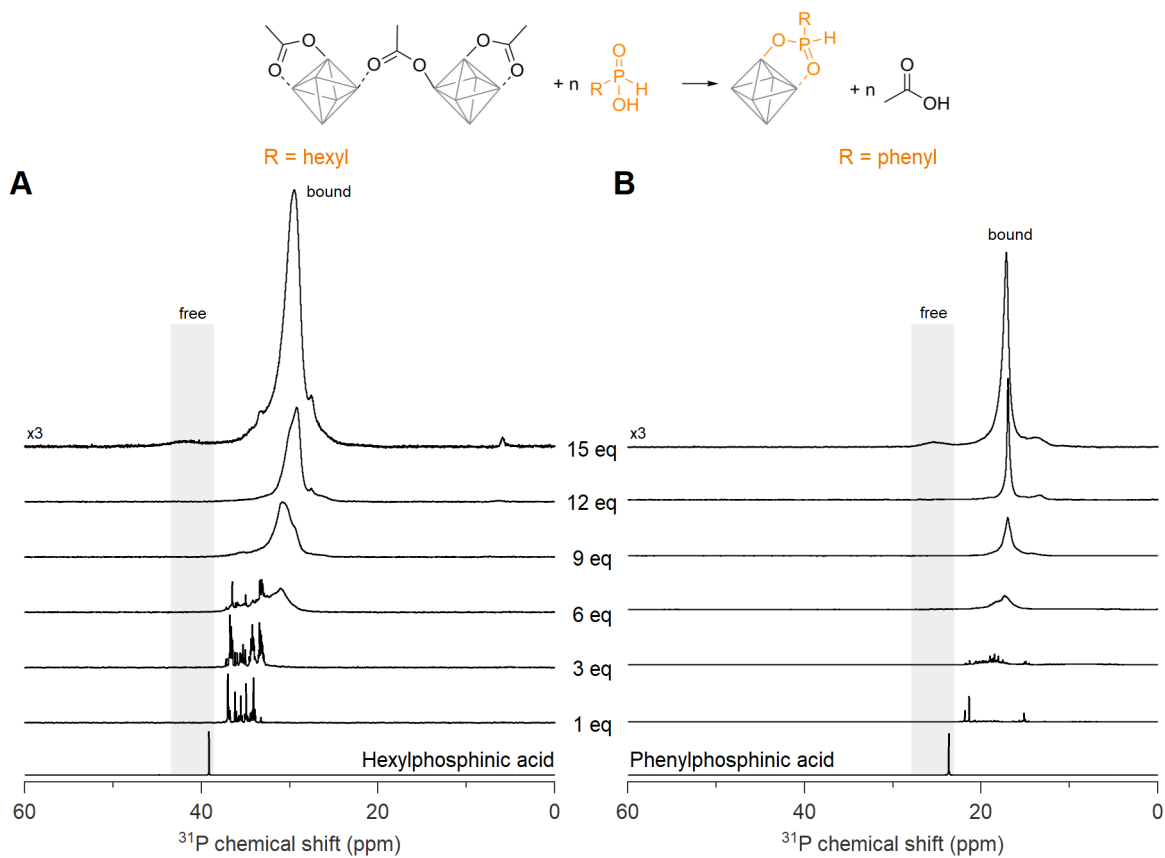


Figure 5: ^{31}P NMR spectra of the titrations of **Zr12**-acetate with phenyl- and hexylphosphonic acid. The cluster concentration is 20 mg/mL in CDCl_3 . ^{31}P NMR spectra of the free phosphonic acids with an equivalent of acetic acid are provided as references.

ppm, pertaining to free acetic acid, remains at the end of the titration. The above results are further generalized with titrations of **Zr12**-acetate with tetradecylphosphonic acid (**Figure S18**) and of **Zr6**-methylbutanoate with hexylphosphonic acid (**Figure S19**). The results are very similar to the ones discussed above, with **Zr6**-methylbutanoate featuring less phosphinate binding modes after the addition of one equivalent of hexylphosphonic acid, as expected for the more symmetrical structure.

Given that monosubstituted phosphonic acids irreversibly exchange all twelve carboxylate ligands, we sought to isolate the fully phosphinate-capped clusters. The **Zr12**-acetate clusters were exchanged with 13.2 equivalents of phenylphosphonic acid in dry DCM at room temperature. The free acetate ligands were removed under vacuum and the phos-

phosphate clusters were purified through precipitation. We obtained single crystals of **Zr6**-phenylphosphate (CCDC-2358676) and **Hf6**-phenylphosphate (CCDC-2358675). Single crystal XRD yielded unprecedented insight into the coordination mode of monoarylphosphate adsorbed onto an oxide surface (see **Figure 6A** and **S31A**). The $M_6O_8H_4^{12+}$ core is preserved with twelve phosphate ligands binding to the cluster in bridging mode. No chelating phosphates were found, in agreement with our DFT calculations, and unlike the reported **Zr6**-benzoate cluster which has both chelating and bridging ligands.⁶⁶ The original cluster dimer was broken up at room temperature since we started from **M12**-acetate and after ligand exchange with phenylphosphonic acid, we obtained the **M6** cluster. Unlike the crystal structure of **Zr6**-benzoate or **Zr12**-acetate, the structure of **Zr6**-phenylphosphate does not contain hydrogen-bonded phosphonic acids. Compared to carboxylate-capped clusters, the metal-metal distances in the core slightly increase (by 1%), along with improved cluster symmetry upon exchange for phosphate ligands (**Figure S54** and **Table S7**). The DFT calculations predicted an expansion of 2%, thus slightly overestimating the core size.

To ensure that the bulk sample has the same structure as the single crystals, we analyzed the bulk powder with X-ray total scattering and PDF analysis (**Figure 6B**). The PDF data was refined using the crystal structure as input model and we obtain a very good fit ($R_w = 0.17$), confirming the sample's structural homogeneity. We could not crystallize **Zr6**-hexylphosphate and thus analyzed its PDF. While the basic features of a **Zr6** cluster are recognized, there are differences in the second Zr-Zr peak (5 Å) and the Zr-P peak at 6.7 Å, indicating a higher degree of disorder in the hexylphosphate-capped cluster. This agrees with the ^{31}P NMR peak width analysis discussed above. We attempted to fit the PDF data of the hexylphosphate-capped cluster with the structure of **Zr6**-phenylphosphate and the result was unsatisfactory (**Figure S45** and **Table S1**). The most significant misfit was observed for the Zr-Zr peak at ~ 5 Å. This peak represents the longest Zr-Zr distance and is the distinctive feature of **Zr6** clusters. Upon detailed examination, we conclude that the peak is split into two distinct peaks, probably due to a highly asymmetric core. For

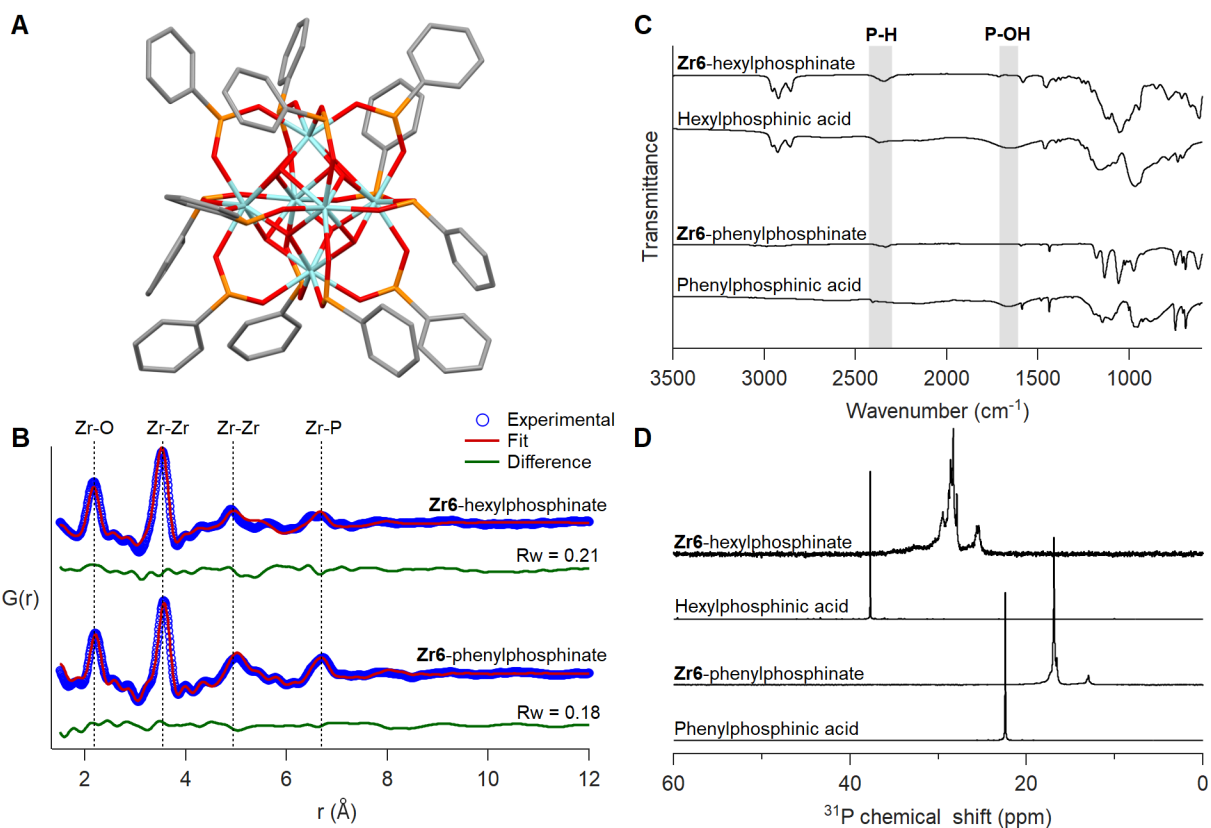


Figure 6: (A) Crystal structure of **Zr₆-phenylphosphinate** cluster - $\text{Zr}_6\text{O}_8\text{H}_4(\text{O}_2\text{PPh})_{12}$. Cyan atoms represent zirconium and all other atoms follow conventional CPK coloring. The co-crystallized dichloromethane molecules and hydrogen atoms are omitted for clarity. (B) PDF fit for **Zr₆-phenylphosphinate** cluster with its crystal structure. PDF fit of **Zr₆-hexylphosphinate** cluster with distorted **Zr₆** phosphinate cluster is also shown. (C) FTIR spectra of **Zr₆** phosphinate clusters. IR spectra of free ligands are also provided for reference. (D) ³¹P NMR of purified **Zr₆** phosphinate clusters. ³¹P NMR of free acids are provided as reference.

the same reason, the Zr-P peak at 6.6 Å is also broader and of lower intensity. We do not detect peaks at higher distances which would be characteristic for a dimer. Dynamic light scattering (DLS) experiments in comparison with **Zr₁₂-hexanoate** clusters confirm that hexylphosphinate-capped clusters are indeed **Zr₆** (**Figure S55-S56**), since the average solvodynamic radius is 0.91 nm for **Zr₁₂-hexanoate** and 0.64 nm for **Zr₆-hexylphosphinate**. We further refined the PDF to identify the most probable structure (**Figure S43**) by moving atoms within a chemically sensible range. The average Zr-Zr, Zr-O, and P-O bond distances in **Zr₆-phenylphosphinate** are 3.58 Å, 2.21 Å and 1.50 Å, respectively, whereas those in the

distorted **Zr6**-phosphinate structure are 3.53 Å, 2.17 Å and 1.47 Å. The asymmetry after core distortion is depicted in **Figure S44**. Similar results are obtained for tetradecylphosphinate-capped clusters (**Figure S46**). The hafnium clusters give identical results, see **Figure S31B, S47, S48** and **Table S2**.

The isolated clusters were also analyzed with FTIR and NMR spectroscopy (**Figure 6C-D**). The references for free phosphinic acid were also given. Upon binding, the broad P-OH stretch ($1500\text{-}1850\text{ cm}^{-1}$) disappears and the P-H stretch (2350 cm^{-1}) remains unaffected. In ^{31}P NMR, the purified clusters feature no resonance of free phosphinic acid. Whereas **Zr6**-phenylphosphinate shows more narrow resonances compared to **Zr6**-hexylphosphinate, the pattern is largely the same: a downfield shoulder to the main peak and a smaller separate resonance upfield. The ^1H NMR spectra show broadened resonances as expected for bound ligands (**Figures S32, S34, S36**).³⁸ Broadening of the bound phosphinate signals in ^1H NMR could mask the acetate ligands that appear around ~ 2.1 ppm in CDCl_3 . To ensure no residual carboxylates are left on the purified phosphinate clusters, ligand stripping experiments with trifluoroacetic acid were performed.⁶⁷ The percentage of acetate ligands found in **Zr6**-hexylphosphinate and **Zr6**-tetradecylphosphinate are 0.4% and 0.07%, respectively, which confirms the complete ligand exchange (**Figure S41-S42**). The purified hafnium clusters showed similar results (**Figure S31C-D, S33, S35, and S37**).

Ligand Exchange with phosphonic acids

Having established that monosubstituted phosphinates are carboxylate mimics with superior binding affinity, we turn to phosphonic acids. When attempting a titration with hexylphosphonic acid, the solution of the **Zr12**-acetate in chloroform immediately formed a gel after the addition of the first equivalent. For 2-ethylhexylphosphonic acid and oleylphosphonic acid, the solution formed a gel after six equivalents (**Figure S20**). Up to six equivalents added, the ^{31}P NMR spectrum (**Figure S22 and S23**) shows resonances of bound phosphonate while the free phosphonic acid (38 ppm) is not detected. Phosphonic acids thus quantitatively

displace carboxylates on oxo clusters. Since the gelation was delayed with increasing steric bulk, we finally titrated **Zr12**-acetate with 2-hexyldecylphosphonic acid.⁴⁵ No visible macroscopic gel was observed and the first equivalent results in two main narrow resonances in the ³¹P NMR spectrum (**Figure 7A**). Upon addition of more phosphonic acid, the resonances broaden, and at 12 equivalents added, the bound phosphonates span a very large chemical shift range (26 ppm), even larger than typical for phosphonate-capped nanocrystals.⁴⁵ ¹H NMR also showed successful replacement of acetate by phosphonate ligands (**Figure S24**). The same gelation behaviour was observed when starting from **Zr6**-methylbutanoate (**Figure S21 and S25**). It is thus independent of the initial cluster structure and only depends on the phosphonate side chain.

Two hypotheses can explain the gelation phenomenon observed: (1) The second acidic group of phosphonic acid connects to a second cluster, resulting in a large disordered network of clusters. (2) the cluster decomposes and forms a new compound. To elucidate more structural information, the exchange product of **Zr12**-acetate with either hexyl or 2-hexyldecyl phosphonic acid, was purified by precipitation or trituration. The hexylphosphonate product was insoluble while the hexyldecylphosphonate product was soluble in organic solvents and showed broad signals in both ¹H and ³¹P NMR (**Figure S38**). We investigated the phosphonate binding mode via infrared spectroscopy. The disappearance of two characteristic broad P-OH vibrations of free phosphonic acids around 2700-2100 cm⁻¹ upon exchanging with clusters confirms their double deprotonation and coordination to the metal (**Figure 7B**).⁶⁸ The three absorption bands in the region 950-1200cm⁻¹ turn into one intense band at 1050 cm⁻¹ upon exchange. The absence of the two flanking bands confirms that the phosphonate binds in tridentate mode.^{69,70} The strong band is assigned to the asymmetric stretch of phosphonate (P=O), and is characteristic for organozirconium phosphonate compounds.⁷¹⁻⁷³ For example, zirconium phenylphosphonate is a layered compound with zirconium and tridentate phosphonate making up one layer and the phenyl substituents separating the layers, see **Figure 7D and S49**. Zirconium phosphonates are not molecular

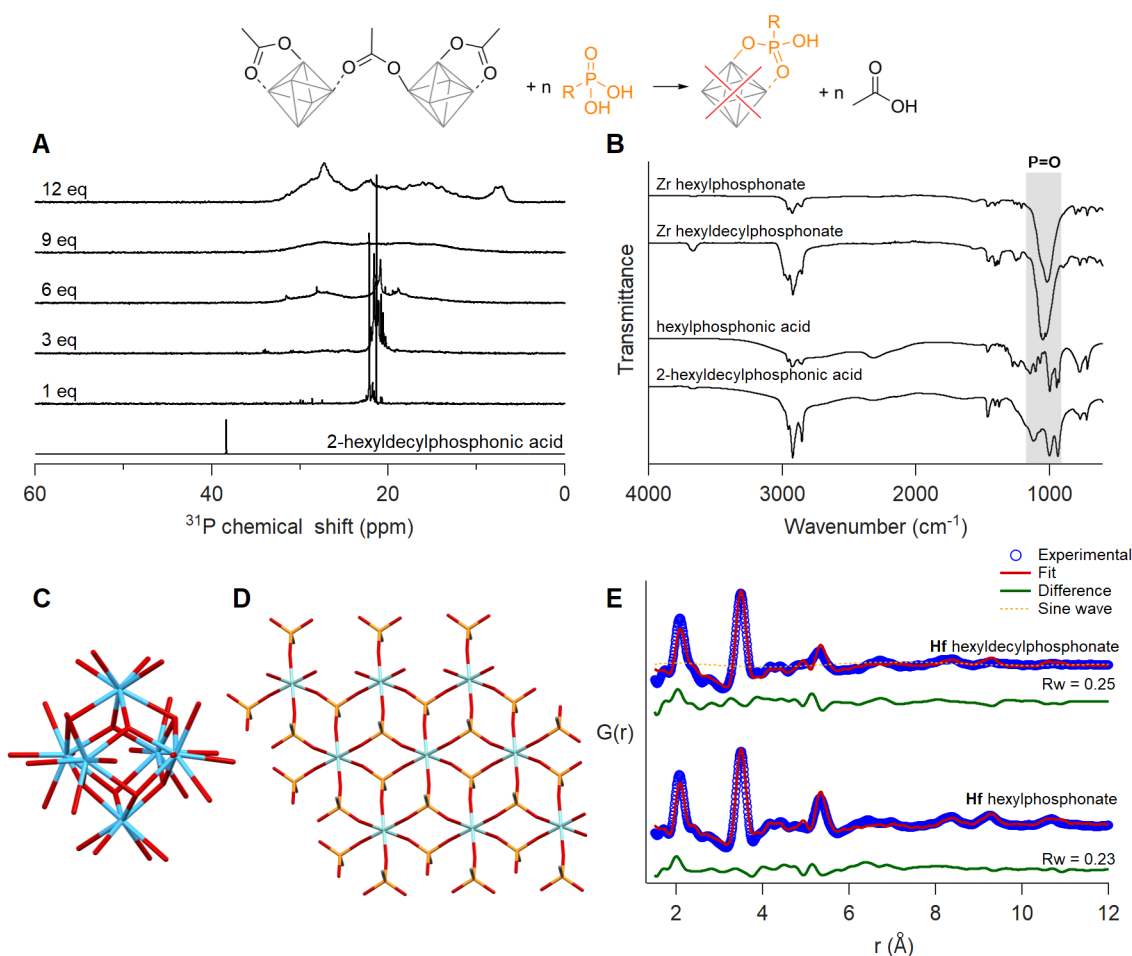


Figure 7: Ligand exchange of **Zr12**-acetate with 2-hexyldecylphosphonic acid. (A) ^{31}P spectra of the titration, with the reference spectrum of 2-hexyldecylphosphonic acid with one equivalent of acetic acid added. The concentration of the cluster was 20 mg/mL in CDCl_3 . (B) IR spectra of phosphonate exchanged zirconium clusters after isolation and purification. IR spectra of free acids are provided as a reference. (C) Structure model of **Hf6** cut from the crystal structure of **Hf12**-acetate. (D) Structure of a 3 x 3 layer zirconium phenylphosphonate (JPCDS:44-2000). Cyan and blue atoms represent zirconium and hafnium, respectively; all other atoms follow conventional CPK coloring. Only the carbon bonded to phosphonate is shown, and the rest of the phenyl ring is omitted for clarity. (E) Dual-phase PDF fit for phosphonate exchanged Hf clusters with a 3 x 3 layer of Hf phenylphosphonate (contains 9 hafnium atoms in total) and **Hf6** chelating bridging acetate.

compounds but extended solids and are generally very insoluble, which would agree with our observation of gel formation.⁷⁴

To improve the signal-to-noise ration, we analyze the PDF of the equivalent phosphonate-exchanged hafnium oxo clusters, due to the large atomic number and high scattering of hafnium. We observe a distinct structural change. The relative intensity of Hf-Hf and Hf-O peaks is too low for a Hf_6O_8 cluster. Therefore, we attempted to fit the experimental PDF with the reported structures of different cluster structures namely, **Zr3**-acetate isopropoxide,⁷⁵ **Zr3**-acetate *tert*-butoxide,⁷⁵ **Zr4**-formate isopropoxide,⁷⁵ **Zr6**-isobutyrate,⁷⁶ **Zr6**-acetate,⁶⁴ **Zr12**-acetate,⁵⁴ **Zr10**-salicylate,⁷⁷ **Zr26**-formate.⁷⁸ For each of these structures, we replaced zirconium with hafnium prior to the fit. All these models showed poor agreement with the experimental data, with a goodness of fit (Rw) ranging from 0.61-0.87 (**Figure S50** and **Table S3**). However, the most prominent peak around 3.5 Å fitted well for cluster models with **Zr6** core or higher. In addition, the atomic distances within the exchanged product align reasonably well with the reported structure of zirconium phenylphosphonate (JCPDS:44-2000, CSD:WEBGEP),⁷⁹ but there is a mismatch in the peak intensities. We fitted the experimental PDF with a single zirconium phenylphosphonate layer (containing 9 zirconium atoms, see **Figure 7D**) and we obtained a poor fit with an Rw of 0.73 (**Figure S51**). Finally, we explored a dual-phase fitting strategy (**Figure 7E**). A comprehensive structure cross-fitting analysis was performed where combinations of two phases were fitted in high throughput. The first phase comprised the zirconium/hafnium phosphonate layers of different sizes (3 x 3 to 7 x 7) and the second phase consisted of the different clusters mentioned above. Out of over 200 combinations, we obtained the best fit where phase I is a 3 x 3 hafnium phosphonate layer and phase II a **Hf6** core, extracted from the crystal structure of **Hf12**-acetate (**Figure 7C**).⁵⁴ Phosphonate exchanged zirconium clusters showed identical results, see **Figure S53** and **Table S5**. This investigation led us to conclude that upon exchanging with phosphonic acids, a significant fraction of Zr/Hf carboxylate clusters loses structural integrity, transforming into metal phosphonates, whereas the rest of the clusters

get trapped in the gel with an intact M_6O_8 core.

Note that the exchange product with 2-hexyldecylphosphonic acid does not form a macroscopic gel. However, dynamic light scattering analysis detected particles with an average solvodynamic diameter of 22.47 nm (**Figure S57**). We thus conclude that the exchange product with 2-hexyldecylphosphonic acid forms amorphous particles of zirconium phosphonate and trapped **Zr6** clusters, and the large steric bulk of the ligand precludes further gelation. Hafnium oxo cluster exchanged with either hexyl or 2-hexyldecylphosphonic acid provide also identical results, see **Figure S40** and **S58**.

Discussion

We conclude from these experimental results that phosphonic acids are not suitable ligands for **Zr6** or **Hf6** oxo clusters. This behavior stands in contrast to the results on oxide nanocrystal surfaces where phosphonic acids were found to be excellent ligands with a high binding affinity. While larger sizes of ZrO_2 crystals (e.g., 3 nm) are stronger, the core of **Zr6** clusters is still prone to restructuring. In addition, on nanocrystals, phosphonic acids were found to behave as monobasic ligands, exchanging only a single carboxylate per phosphonic acid equivalent.^{46,52,80,81} Interestingly for colloidal InP clusters, di-anionic binding of phosphonate was reported.⁸² For the few clusters with phosphonate ligands reported in the literature, the phosphonate is always present as a tridentate ligand. However, these are not **Zr6** clusters but rather two $Zr_3O(\mu_2-OR)_3(OR)_3$ units bridged by four phosphonates.^{55,56} Such a structure can be regarded as the first step of the decomposition of the **Zr6** clusters where the two **Zr3** units are pushed apart. The tridentate coordination of phosphonates was not considered in our theoretical calculations, neither was the decomposition of the oxo cluster. In the absence of experiments, one could have concluded that phosphonates were the most desirable ligands for oxo clusters. This shows how our own bias and the limited scope of theoretical calculations need to be carefully considered. Finally, while Zr MOFs with

phosphonate ligands are highly desired because of their superior stability, it is frequently hypothesized that they are difficult to make due to the poor reversibility of the phosphonate coordination bond.⁸³ However, here we exposed the real reason; the Zr_6O_8 oxo cluster core is unstable in the presence of phosphonic acids.

Disubstituted phosphinic acids were also not suitable ligands to fully coordinate **Zr6** oxo clusters since they are too sterically hindered. Only mixed ligand shells with less sterically hindered carboxylates are possible. Given that space is even more limited on flatter nanocrystal surfaces, we also suggest that they are also poor ligands for nanocrystals. In the absence of stronger ligands, they can still bind, albeit with a lower ligand density.⁴⁸ Monosubstituted phosphinic acids are the most promising ligands for oxo clusters. They are monobasic, and their binding mode is highly similar to that of carboxylates, with the difference that phosphinates prefer the bridging over the chelating mode.

Conclusion

We have studied ligand exchange on atomically precise oxo clusters both computationally and experimentally. We find that phosphinates/phosphonates exhibit superior binding affinity compared to carboxylates. However, dialkylphosphinic acids can only partially cover the cluster surface due to sterical hindrance, which results in mixed-ligand shells. Monoalkyl- and monoarylphosphinates can quantitatively displace all carboxylates to yield fully phosphinate-capped clusters. We reported the crystal structures of the first phosphinate-capped zirconium and hafnium oxo clusters. Ligand exchange for phosphonates causes the partial structural reorganization of clusters to form metal phosphonates, ultimately forming a macroscopic or nanoscopic gel, depending on the sterical hindrance of the phosphonic acid. Even though metal oxo clusters are promising prototypes for oxide nanocrystals, we here identified important differences in their surface chemistries. Some insights are however transferable, for example the composition-dependent thermodynamics of ligand binding. Finally, these results

gave important insights in MOFs syntheses and delineate the limited synthetic feasibility of Zr-phosphonate MOFs.

Methods

Materials

All chemical reagents and solvents were purchased from commercial sources and unless mentioned, used as received without further purification. Zirconium *n*-propoxide (70 w% in 1-propanol) and hafnium *n*-butoxide (99%) were purchased from Sigma-Aldrich and stored in a Straus flask upon arrival. Acetic acid (>99%) was purchased from Sigma-Aldrich and vacuum distilled to remove the water content. Methylbutanoic acid (98%), and hexylphosphonic acid (98%) were received from Sigma-Aldrich. Dry dichloromethane (99.8%), dry methanol (99.8%), dry tetrahydrofuran (99.5%), oleic acid (90%), and bromotrimethylsilane (98%) were purchased from Thermo Fisher Scientific. Acetone (100%), acetonitrile (99.9%), diethyl ether (99.5%), tetrahydrofuran (99.7%), anhydrous sodium sulfate (98%), and sodium hydroxide (97%) were obtained from VWR Chemicals. Lithium aluminium hydride (95%), Celite[®]545, triphenylphosphine (99%), sodium hypophosphite monohydrate (99%), potassium bisulfate, hexane (>97%), and dichloromethane (99.8%) were received from Sigma-Aldrich. Hexane (99%) and ethanol were bought from Honeywell Research Chemicals and Biosolve, respectively. 1-hexene (97%), 1-tetradecene (90%), tetrabromomethane (99%), and triethylborane (1 M in THF, 11%) were purchased from TCI Chemicals. Diethylphosphinic acid (97%) was received from BLDPharm. Deuterated chloroform (CDCl₃, 99.8%) was received from Eurisotop and treated with 4 Å molecular sieves (Sigma-Aldrich) for 24 hours before use. Milli-Q[®] water (resistivity of 18.2 MΩcm at 25 °C) was dispensed from Merck Millipore Advantage A10 Water Purification System with Qpod. For size exclusion chromatography, Bio-Beads S-X3 was purchased from BIO-RAD.

General instrumentation

Nuclear magnetic resonance (NMR) spectra were recorded at 298.15K on a Bruker UltraShield 500 spectrometer operating at a ^1H frequency of 500.13 MHz. Regular ^1H and ^{31}P NMR spectra were acquired using the standard pulse sequences with a 30 degree pulse with a recycle delay of 1.5 and 1.0 second from the Bruker library; zg30, zgpg30 respectively. ^1H NMR spectra were acquired with 64 scans and post-processed with a line broadening of 1 Hz. $^{31}\text{P}\{^1\text{H}\}$ NMR spectra were acquired using inverse gated decoupling with 4096 scans, and processed with a line broadening of 2 Hz to reduce noise. All resonances are background-corrected. Chemical shifts (δ) are given in parts per million (ppm), and the residual solvent peak was used as an internal standard (CDCl_3 : $\delta\text{H} = 7.26$ ppm). The chemical shifts for other nuclei were referenced indirectly to the ^1H NMR frequency of the sample with the “xiref”-macro in Bruker. The IR spectra were recorded on a PerkinElmer spectrum 2 ATR-FTIR with a diamond crystal.

Synthesis of Zr/Hf clusters, phosphonic and phosphinic acids

The **Zr12**-acetate ($\text{Zr}_{12}\text{O}_{16}\text{H}_8(\text{OOCMe})_{24} \cdot 6 \text{ MeCOOH} \cdot 3.5 \text{ CH}_2\text{Cl}_2$), **Hf12**-acetate ($\text{Hf}_{12}\text{O}_{16}\text{H}_8(\text{OOCMe})_{24} \cdot 6 \text{ MeCOOH} \cdot 3 \text{ CH}_2\text{Cl}_2$) and **Zr6**-methylbutanoate clusters ($\text{Zr}_6\text{O}_8\text{H}_4(\text{OOCCH}(\text{CH}_3)\text{C}_2\text{H}_5)_{12}$) were synthesized according to Van den Eynden *et al.*¹² 2-ethylhexyl, 2-hexyldecyl and oleylphosphonic acids were synthesized according to the literature.^{45,46} Dioctylphosphinic acid was synthesized according to the procedure described by Wang *et al.*⁸⁴ Phosphinic acid ligands (hexyl, tetradecyl) were synthesized according to the procedures of Dhaene *et al.*⁶⁵

Ligand exchange titrations

10-12 mg of **Zr12**-acetate cluster was dissolved in 500 μL CDCl_3 in an NMR tube with moderate heating. In a second vial, 24 equivalents of phosphonic/phosphinic acid were

dissolved in 120 μL CDCl_3 . 10 μL of the acid solution (2 equivalents per **Zr12**, 1 equivalent per **Zr6** core) was added each time to the acetate cluster solution, and NMR (^1H & ^{31}P) spectra were recorded.

Ligand exchange reactions

Zr6-phenylphosphinate cluster: 500 mg (0.146 mmol, 1 eq.) of **Zr12**-acetate cluster was suspended in 10 mL dry dichloromethane in a glass vial. 546.47 mg (3.85 mmol, 1.1 eq. per acetate) of phenylphosphinic acid was added and stirred overnight at room temperature. The addition of phenylphosphinic acid made the cluster soluble in DCM. After the completion of the reaction, the mixture was evaporated under vacuum, dissolved in 5 mL of dry dichloromethane, stirred for 4 hours, and the product was precipitated with hexane. The precipitation was cycled thrice and finally, the product was dried in vacuo. Yield: 396.1 mg (57%). Crystallization: The crystals were obtained through vapor diffusion technique. ~ 25 mg of zirconium phenylphosphinate cluster was dissolved in 0.2 mL dry dichloromethane in a small vial. The vial was placed in a larger vial with 5 mL hexane, closed the lid, and kept undisturbed for over a week to obtain single crystals.

Hf6-phenylphosphinate cluster: 100 mg (0.023 mmol, 1 eq.) of **Hf12**-acetate cluster was suspended in 2 mL dry dichloromethane in a glass vial. 84.5 mg (0.60 mmol, 1.1 eq. per acetate) of phenylphosphinic acid was added and stirred overnight at room temperature. The addition of phenylphosphinic acid made the cluster soluble in DCM. After the completion of the reaction, the mixture was evaporated under vacuum, dissolved in 3 mL of dry dichloromethane, and the product was precipitated with hexane. The precipitation was cycled thrice and finally, the product was dried in vacuo. Yield: 91.7 mg (70%). Crystallization: The crystals were obtained through vapor diffusion technique. ~ 25 mg of hafnium phenylphosphinate cluster was dissolved in 0.2 mL dry dichloromethane in a small vial. The vial was placed in a larger vial with 5 mL pentane, closed the lid, and kept undisturbed for over a week to obtain single crystals.

Zr6-hexylphosphinate cluster: 200 mg (0.058 mmol, 1 eq.) of **Zr12**-acetate cluster was suspended in 4 mL dry dichloromethane in a glass vial. 231 mg (1.54 mmol, 1.1 eq. per acetate) of hexylphosphinic acid was added and stirred overnight at room temperature. The addition of hexylphosphinic acid made the cluster soluble in DCM. After the completion of the reaction, the mixture was evaporated under vacuum, followed by the addition of 2 mL dry DCM and stirring for 4 hours (equilibration). To remove excess ligands, the mixture was concentrated, and the solid was suspended in 2 mL acetonitrile, stirred overnight, collected through centrifugation, and dried in vacuo to obtain a white solid. Yield: 99 mg

To remove H-bonded carboxylates, 0.5 equivalents of hexylphosphinic acid can be additionally added along with dry DCM while equilibration. Since the excess phosphinate makes the cluster soluble in acetonitrile, trituration-based purification is not possible. So final purification was performed with size exclusion chromatography. 15 g of Bio-Beads S-X3 was soaked in DCM overnight and subsequently packed in a column. 20 mg of the crude dissolved in 0.5 mL DCM was eluted.

Hf6-hexylphosphinate cluster: 200 mg (0.045 mmol, 1 eq.) of **Hf12**-acetate cluster was suspended in 4 mL dry dichloromethane in a glass vial. 178.6 mg (1.19 mmol, 1.1 eq. per acetate) of hexylphosphinic acid was added and stirred overnight at room temperature. The addition of hexylphosphinic acid made the cluster soluble in DCM. After the completion of the reaction, the mixture was evaporated under vacuum, followed by the addition of 2 mL dry DCM and stirring for 4 hours. To remove excess ligands, the mixture was concentrated, and the solid was suspended in 2 mL acetonitrile, stirred overnight, collected through centrifugation, and dried in vacuo to obtain a white solid. Yield: 299 mg

Zr6-tetradecylphosphinate cluster: 200 mg (0.058 mmol, 1 eq.) of **Zr12**-acetate cluster was suspended in 4 mL dry dichloromethane in a glass vial. 404 mg (1.54 mmol, 1.1 eq. per acetate) of tetradecylphosphinic acid was added and stirred overnight at room temperature. The addition of tetradecylphosphinic acid made the cluster soluble in DCM. After the completion of the reaction, the mixture was evaporated under vacuum, followed

by the addition of 2 mL dry DCM and stirring for 4 hours. The product was precipitated with acetonitrile. The precipitation was cycled thrice, and finally, the product was dried in vacuo. Yield: 215 mg

To remove H-bonded carboxylates, 0.5 equivalents of tetradecylphosphinic acid can be additionally added along with dry DCM while equilibration.

Hf6-tetradecylphosphinate cluster: 200 mg (0.045 mmol, 1 eq.) of **Hf12**-acetate cluster was suspended in 4 mL dry dichloromethane in a glass vial. 178.6 mg (1.19 mmol, 1.1 eq. per acetate) of tetradecylphosphinic acid was added and stirred overnight at room temperature. The addition of tetradecylphosphinic acid made the cluster soluble in DCM. After the completion of the reaction, the mixture was evaporated under vacuum, followed by the addition of 2 mL dry DCM and stirring for 4 hours. The product was precipitated with acetonitrile. The precipitation was cycled thrice and finally, the product was dried in vacuo. Yield: 329 mg

Zr hexylphosphonate: 200 mg (0.058 mmol, 1 eq.) of **Zr12**-acetate cluster was suspended in 4 mL dry dichloromethane in a glass vial. 256 mg (1.54 mmol, 1.1 eq. per acetate) of hexylphosphonic acid was added. Though the mixture gelled immediately, the stirring was continued overnight at room temperature. After the completion of the reaction, the mixture was evaporated under vacuum, followed by the addition of 2 mL dry DCM and stirring for 4 hours. To remove excess ligands, the mixture was concentrated, and the solid was suspended in 5 mL acetonitrile, stirred overnight, collected through centrifugation, and dried in vacuo to obtain a white solid. Yield: 249 mg

Hf hexylphosphonate: 200 mg (0.045 mmol, 1 eq.) of **Hf12**-acetate cluster was suspended in 4 mL dry dichloromethane in a glass vial. 198 mg (1.19 mmol, 1.1 eq. per acetate) of hexylphosphonic acid was added. Though the mixture gelled immediately, the stirring was continued overnight at room temperature. After the completion of the reaction, the mixture was evaporated under vacuum, followed by the addition of 2 mL dry DCM and stirring for 4 hours. To remove excess ligands, the mixture was concentrated, and the solid was suspended

in 5 mL acetonitrile, stirred overnight, collected through centrifugation, and dried in vacuo to obtain a white solid. Yield: 287 mg

Zr hexyldecylphosphonate: 200 mg (0.058 mmol, 1 eq.) of **Zr12**-acetate cluster was suspended in 4 mL dry dichloromethane in a glass vial. 471 mg (1.54 mmol, 1.1 eq. per acetate) of 2-hexyldecylphosphinic acid dissolved in 2 mL dry dichloromethane was added and stirred overnight at room temperature. The addition of 2-hexyldecylphosphinic acid made the cluster soluble in DCM. After the completion of the reaction, the mixture was evaporated under vacuum to remove exchanged free acetic acid. The solid was redissolved in 2 mL of dry dichloromethane and stirred for 4 hours, and finally, the product was precipitated with acetone. The precipitation was cycled three times, and the product was dried under vacuum to yield a white solid. Yield: 395 mg

Hf hexyldecylphosphonate: 200 mg (0.045 mmol, 1 eq.) of **Hf12**-acetate cluster was suspended in 4 mL dry dichloromethane in a glass vial. 377 μL (1.19 mmol, 1.1 eq. per acetate) of 2-hexyldecylphosphinic acid dissolved in 2 mL dry dichloromethane was added and stirred overnight at room temperature. The addition of 2-hexyldecylphosphinic acid made the cluster soluble in DCM. After the completion of the reaction, the mixture was evaporated under vacuum to remove exchanged free acetic acid. The solid was redissolved in 2 mL of dry dichloromethane and stirred for 4 hours, and finally, the product was precipitated with acetone. The precipitation was cycled three times, and the product was dried under vacuum to yield a white solid. Yield: 386 mg

Dynamic light scattering analysis

Dynamic light scattering (DLS) measurements were performed on a Malvern Zetasizer Ultra Dynamic Light Scattering system in backscattering mode. 10 mg/mL solutions of clusters in chloroform after syringe filtering (PTFE 0.2 μm) were subjected to the analysis in a glass cuvette. All measurements were performed in triplicate at 25 °C after equilibrating inside the system for 240 seconds and the sample concentration was tuned to achieve system attenuator

values between 9-10. For **Zr6**-hexylphosphinate and **Zr12**-hexanoate clusters, fitting was performed according to Van den Eynden *et al.*⁸⁵

Ligand stripping experiments

20 mg of the cluster was dissolved in 400 μL CDCl_3 . 100 μL of trifluoroacetic acid was added to the solution. The mixture was centrifuged, the supernatant was collected, and NMR (^1H and ^{31}P) was recorded.

DFT calculations

Computational calculations were performed with the CP2K program package.⁸⁶ Cell parameters were optimized at the DFT level of theory with the hybrid Gaussian and plane waves (GPW) formalism and the Perdew-Burke-Ernzerhof (PBE) functionals.⁸⁷ Goedecker-Teter-Hutter (GTH) pseudopotentials⁸⁸ and the standard double- ζ MOLOPT basis sets (DZVP-MOLOPT-SR-GTH)⁸⁹ have been used for all the atoms (Zr, Hf, C, H, O and P). The cutoff for the plane wave representation of electron density was set to 400 Ry, while the SCF convergence criterion was set to 1×10^{-6} . All CP2K calculations were performed in vacuum without periodic boundary conditions using Wavelet Poisson solver.⁹⁰ A box of $22 \times 22 \times 22 \text{ \AA}$ was used for **Zr6** (dimensions: $12 \times 12 \times 12 \text{ \AA}$), whereas a box of $33 \times 33 \times 33 \text{ \AA}$ was employed for **Zr12**- (dimensions: $17 \times 22 \times 23 \text{ \AA}$) to achieve a zero electronic density at the edge of the box. The enthalpy of ligand exchange reactions was calculated as the difference between optimized energies of products and reactants in a balanced chemical equation. The bond lengths and bond angles of the optimized structures were extracted using the 'xyz2tab' Python code.⁹¹

Synchrotron X-ray total scattering experiments.

Samples were prepared in 1 mm polyimide kapton tube and were measured either at beamline 11-ID-BM at Advanced Photon Source, Argonne National Laboratory, USA, 28-ID-2 at National Synchrotron Light Source II, Brookhaven National Laboratory, USA or at beamline P21.1 at DESY in Hamburg, Germany. X-ray total scattering data were collected at room temperature in rapid acquisition mode, using a Perkin Elmer digital X-ray flat panel amorphous silicon detector (2048×2048 pixels and $200 \times 200 \mu\text{m}$ pixel size) with a sample-to-detector distance of 180 mm (11-ID-BM), 267 mm (28-ID-2) or 380 mm (P21.1). The incident wavelength of the X-rays was $\lambda = 0.2110 \text{ \AA}$ (11-ID-BM), 0.1821 \AA (28-ID-2) or 0.1220 \AA (P21.1). Calibration of the experimental setup was performed using a Ni standard.

Analysis of synchrotron X-ray total scattering data.

Raw 2D data were corrected for geometrical effects and polarization, then azimuthally integrated to produce 1D scattering intensities versus the magnitude of the momentum transfer Q (where $Q = 4\pi\sin\theta/\lambda$ for elastic scattering) using pyFAI and xpdtools.^{92,93} The program xPDFsuite with PDFgetX3 was used to perform the background subtraction, further corrections, and normalization to obtain the reduced total scattering structure function $F(Q)$, and Fourier transformation to obtain the pair distribution function (PDF), $G(r)$.^{94,95} For data reduction, the following parameters were used after proper background subtraction: $Q_{\text{min}} = 0.8 \text{ \AA}^{-1}$, $Q_{\text{max}} = 22 \text{ \AA}^{-1}$, $R_{\text{poly}} = 0.9 \text{ \AA}$. Modeling and fitting were carried out using Diffpy-CMI.⁹⁶ The Debye scattering equation was used to generate the calculated PDF from discrete structure models. The structure models are supplied as xyz files in the supporting information. The refinements were carried out by refining the scale factor, isotropic atomic displacement parameters (Uiso), and delta2 (coefficient for $1/r^2$ contribution to the peak sharpening). The exponentially dampening sine-wave contribution was calculated according to the following equation.

$$y = A e^{-\left(\frac{r-r_0}{2\sigma_{\text{eff}}}\right)^2} \sin\left(2\pi\left(\frac{r}{\lambda} - \phi\right)\right)$$

A - Amplitude of oscillation, r - the distance in PDF, λ - wavelength, ϕ - phase shift, σ - effective dampening with $\sigma_{\text{eff}} = \sigma / a$ for $r < r_0$ and $\sigma_{\text{eff}} = \sigma \times a$ for $r > r_0$, a is the asymmetry parameter. r_0 is not a physical parameter in real space and is used to describe different dampening behavior.⁹⁷

Acknowledgement

The authors thank the Swiss Nanoscience Institute (Project P2006) and the SNF NCCR molecular systems engineering (182895) for funding. Ivan Infante thanks the EU for the Horizon Europe EIC Pathfinder program through project 101098649–UNICORN. Quantum chemical calculations were performed at sciCORE (<http://scicore.unibas.ch/>) scientific computing center at the University of Basel. This research used resources of the Advanced Photon Source, a U.S. Department of Energy (DOE) Office of Science user-operated facility for the DOE Office of Science by the Argonne National Laboratory under Contract No. DE-AC02-06CH11357. We would like to thank Dr. Leighanne Gallington for assistance in using beamline 11-ID-B (proposal: GUP-81183). This research used resources of beamline 28-ID-2 of the National Synchrotron Light Source II, a U.S. Department of Energy (DOE) Office of Science User Facility operated for the DOE Office of Science by Brookhaven National Laboratory under Contract No. DE-SC0012704. We would like to thank Dr. Sanjit K. Ghose and Dr. Hui Zhong for their assistance in using the beamline for PDF acquisition. Beamtime was allocated for proposal number 313157. We acknowledge DESY (Hamburg, Germany), a member of the Helmholtz Association HGF, for the provision of experimental facilities. Parts of this research were carried out at PETRA III, and we would like to thank Dr. Ann-Christin Dippel for assistance in using beamline P21.1. Beamtime was allocated for Proposal I-20231114 EC.

Supporting Information Available

Details of DFT calculations, NMR titrations, Ligand stripping experiments, NMR, FTIR and DLS data of purified compounds, PDF refinements, Crystallographic data of new metal oxo clusters

References

- (1) Dan-Hardi, M.; Serre, C.; Frot, T.; Rozes, L.; Maurin, G.; Sanchez, C.; Férey, G. A New Photoactive Crystalline Highly Porous Titanium(IV) Dicarboxylate. *J. Am. Chem. Soc.* **2009**, *131*, 10857–10859.
- (2) Cavka, J. H.; Jakobsen, S.; Olsbye, U.; Guillou, N.; Lamberti, C.; Bordiga, S.; Lillerud, K. P. A New Zirconium Inorganic Building Brick Forming Metal Organic Frameworks with Exceptional Stability. *J. Am. Chem. Soc.* **2008**, *130*, 13850–13851.
- (3) Fidelli, A. M.; Karadeniz, B.; Howarth, A. J.; Huskić, I.; Germann, L. S.; Halasz, I.; Etter, M.; Moon, S.-Y.; Dinnebier, R. E.; Stilinović, V.; Farha, O. K.; Friščić, T.; Užarević, K. Green and rapid mechanosynthesis of high-porosity NU- and UiO-type metal–organic frameworks. *Chem. Commun.* **2018**, *54*, 6999–7002.
- (4) Dai, S.; Simms, C.; Dovgaliuk, I.; Patriarche, G.; Tissot, A.; Parac-Vogt, T. N.; Serre, C. Monodispersed MOF-808 Nanocrystals Synthesized via a Scalable Room-Temperature Approach for Efficient Heterogeneous Peptide Bond Hydrolysis. *Chem. Mater.* **2021**, *33*, 7057–7066.
- (5) Bezrukov, A. A.; Törnroos, K. W.; Le Roux, E.; Dietzel, P. D. C. Incorporation of an intact dimeric Zr₁₂ oxo cluster from a molecular precursor in a new zirconium metal–organic framework. *Chem. Commun.* **2018**, *54*, 2735–2738.

- (6) Schubert, U. Polymers Reinforced by Covalently Bonded Inorganic Clusters. *Chem. Mater.* **2001**, *13*, 3487–3494.
- (7) Gross, S. Oxocluster-Reinforced Organic–Inorganic Hybrid Mater.: Effect of Transition Metal Oxoclusters on Structural and Functional Properties. *J. Mater. Chem.* **2011**, *21*, 15853–15861.
- (8) Murali, M.; Berne, D.; Joly-Duhamel, C.; Caillol, S.; Leclerc, E.; Manoury, E.; Ladmiral, V.; Poli, R. Coordination Adaptable Networks: Zirconium(IV) Carboxylates. *Chem. Eur. J.* **2022**, *28*, e202202058.
- (9) Faccioli, F.; Bauer, M.; Pedron, D.; Sorarù, A.; Carraro, M.; Gross, S. Hydrolytic Stability and Hydrogen Peroxide Activation of Zirconium-Based Oxoclusters. *Eur. J. Inorg. Chem.* **2015**, *2015*, 210–225.
- (10) Moons, J.; de Azambuja, F.; Mihailovic, J.; Kozma, K.; Smiljanic, K.; Amiri, M.; Cirkovic Velickovic, T.; Nyman, M.; Parac-Vogt, T. N. Discrete Hf₁₈ Metal-oxo Cluster as a Heterogeneous Nanozyme for Site-Specific Proteolysis. *Angew. Chem. Int. Ed.* **2020**, *59*, 9094–9101.
- (11) Zhang, Y.; de Azambuja, F.; Parac-Vogt, T. N. Zirconium oxo clusters as discrete molecular catalysts for the direct amide bond formation. *Catal. Sci. Technol.* **2022**, *12*, 3190–3201.
- (12) Van den Eynden, D.; Pokratath, R.; Mathew, J. P.; Goossens, E.; De Buysser, K.; De Roo, J. Fatty acid capped, metal oxo clusters as the smallest conceivable nanocrystal prototypes. *Chem. Sci.* **2023**, *14*, 573–585.
- (13) Pulparayil Mathew, J.; Seno, C.; Jaiswal, M.; Simms, C.; Reichholf, N.; Van den Eynden, D.; Parac-Vogt, T. N.; De Roo, J. The Central Role of Oxo Clusters in Zirconium- and Hafnium-Based Esterification Catalysis. *ChemRxiv* **2024**,

- (14) Van den Eynden, D.; Pokratath, R.; De Roo, J. Nonaqueous Chemistry of Group 4 Oxo Clusters and Colloidal Metal Oxide Nanocrystals. *Chem. Rev.* **2022**, *122*, 10538–10572.
- (15) Schubert, U. Surface chemistry of carboxylato-substituted metal oxo clusters – Model systems for nanoparticles. *Coord. Chem. Rev.* **2017**, *350*, 61–67.
- (16) Kickelbick, G.; Schubert, U. Oxozirconium Methacrylate Clusters: $Zr_6(OH)_4O_4(OMc)_{12}$ and $Zr_4O_2(OMc)_{12}$ (OMc = Methacrylate). *Ber. Dtsch. Chem. Ges.* **1997**, *130*, 473–478.
- (17) Murali, M.; Bijani, C.; Daran, J.-C.; Manoury, E.; Poli, R. Acetate exchange mechanism on a Zr_{12} oxo hydroxo cluster: relevance for reshaping Zr–carboxylate coordination adaptable networks. *Chem. Sci.* **2023**, *14*, 8152–8163.
- (18) Choi, J. I.; Moon, D.; Chun, H. Static and Dynamic Adsorptions of Water Vapor by Cyclic $[Zr_{36}]$ Clusters: Implications for Atmospheric Water Capture Using Molecular Solids. *Bull. Korean Chem. Soc* **2021**, *42*, 294–302.
- (19) Zhang, Y.; de Azambuja, F.; Parac-Vogt, T. N. The forgotten chemistry of group(IV) metals: A survey on the synthesis, structure, and properties of discrete Zr(IV), Hf(IV), and Ti(IV) oxo clusters. *Coord. Chem. Rev.* **2021**, *438*, 213886.
- (20) Mereacre, V.; Ako, A. M.; Akhtar, M. N.; Lindemann, A.; Anson, C. E.; Powell, A. K. Homo- and Heterovalent Polynuclear Cerium and Cerium/Manganese Aggregates. *Helv. Chim. Acta* **2009**, *92*, 2507–2524.
- (21) Takao, S.; Takao, K.; Kraus, W.; Emmerling, F.; Scheinost, A. C.; Bernhard, G.; Hennig, C. First Hexanuclear UIV and ThIV Formate Complexes – Structure and Stability Range in Aqueous Solution. *Eur. J. Inorg. Chem.* **2009**, *2009*, 4771–4775.
- (22) Das, R.; Sarma, R.; Baruah, J. B. A hexanuclear cerium(IV) cluster with mixed coordination environment. *Inorg. Chem. Commun.* **2010**, *13*, 793–795.

- (23) Knope, K. E.; Wilson, R. E.; Vasiliu, M.; Dixon, D. A.; Soderholm, L. Thorium(IV) Molecular Clusters with a Hexanuclear Th Core. *Inorg. Chem.* **2011**, *50*, 9696–9704.
- (24) Frot, T.; Cochet, S.; Laurent, G.; Sassoie, C.; Popall, M.; Sanchez, C.; Rozes, L. $\text{Ti}_8\text{O}_8(\text{OOCR})_{16}$, a New Family of Titanium–Oxo Clusters: Potential NBUs for Reticular Chemistry. *Eur. J. Inorg. Chem.* **2010**, *2010*, 5650–5659.
- (25) Hong, K.; Bak, W.; Chun, H. Robust Molecular Crystals of Titanium(IV)-oxo-Carboxylate Clusters Showing Water Stability and CO_2 Sorption Capability. *Inorg. Chem.* **2014**, *53*, 7288–7293.
- (26) Turkevich, J.; Stevenson, P. C.; Hillier, J. A study of the nucleation and growth processes in the synthesis of colloidal gold. *Discuss. Faraday Soc.* **1951**, *11*, 55–75.
- (27) Brust, M.; Walker, M.; Bethell, D.; Schiffrin, D. J.; Whyman, R. Synthesis of thiol-derivatised gold nanoparticles in a two-phase Liquid–Liquid system. *J. Chem. Soc., Chem. Commun.* **1994**, 801–802.
- (28) Lee, P. C.; Meisel, D. Adsorption and surface-enhanced Raman of dyes on silver and gold sols. *J. Phys. Chem.* **1982**, *86*, 3391–3395.
- (29) Kang, H.; Buchman, J. T.; Rodriguez, R. S.; Ring, H. L.; He, J.; Bantz, K. C.; Haynes, C. L. Stabilization of Silver and Gold Nanoparticles: Preservation and Improvement of Plasmonic Functionalities. *Chem. Rev.* **2019**, *119*, 664–699.
- (30) Murray, C. B.; Norris, D. J.; Bawendi, M. G. Synthesis and characterization of nearly monodisperse CdE (E = S, Se, Te) semiconductor nanocrystallites. *J. Am. Chem. Soc.* **1993**, *115*, 8706–8715.
- (31) Efros, A. L.; Brus, L. E. Nanocrystal Quantum Dots: From Discovery to Modern Development. *ACS Nano* **2021**, *15*, 6192–6210.

- (32) Niederberger, M.; Garnweitner, G. Organic reaction pathways in the nonaqueous synthesis of metal oxide nanoparticles. *Chem. Eur. J.* **2006**, *12*, 7282–7302.
- (33) Shim, M.; Guyot-Sionnest, P. n-type colloidal semiconductor nanocrystals. *Nature* **2000**, *407*, 981–983.
- (34) Yuan, M.; Liu, M.; Sargent, E. H. Colloidal quantum dot solids for solution-processed solar cells. *Nat. Energy* **2016**, *1*, 16016.
- (35) Frederix, F.; Friedt, J.-M.; Choi, K.-H.; Laureyn, W.; Campitelli, A.; Mondelaers, D.; Maes, G.; Borghs, G. Biosensing Based on Light Absorption of Nanoscaled Gold and Silver Particles. *Anal. Chem.* **2003**, *75*, 6894–6900.
- (36) Zimmer, J. P.; Kim, S.-W.; Ohnishi, S.; Tanaka, E.; Frangioni, J. V.; Bawendi, M. G. Size Series of Small Indium Arsenide-Zinc Selenide Core-Shell Nanocrystals and Their Application to In Vivo Imaging. *J. Am. Chem. Soc.* **2006**, *128*, 2526–2527.
- (37) Wang, W.; Zhang, M.; Pan, Z.; Biesold, G. M.; Liang, S.; Rao, H.; Lin, Z.; Zhong, X. Colloidal Inorganic Ligand-Capped Nanocrystals: Fundamentals, Status, and Insights into Advanced Functional Nanodevices. *Chem. Rev.* **2022**, *122*, 4091–4162.
- (38) De Roo, J. The Surface Chemistry of Colloidal Nanocrystals Capped by Organic Ligands. *Chem. Mater.* **2023**, *35*, 3781–3792.
- (39) Yin, Y.; Alivisatos, A. P. Colloidal nanocrystal synthesis and the organic-inorganic interface. *Nature* **2005**, *437*, 664–670.
- (40) De Roo, J. Chemical Considerations for Colloidal Nanocrystal Synthesis. *Chem. Mater.* **2022**, *34*, 5766–5779.
- (41) De Roo, J.; Van den Broeck, F.; De Keukeleere, K.; Martins, J. C.; Van Driessche, I.; Hens, Z. Unravelling the Surface Chemistry of Metal Oxide Nanocrystals, the Role of Acids and Bases. *J. Am. Chem. Soc.* **2014**, *136*, 9650–9657.

- (42) De Roo, J.; Justo, Y.; De Keukeleere, K.; Van den Broeck, F.; Martins, J. C.; Van Driessche, I.; Hens, Z. Carboxylic-Acid-Passivated Metal Oxide Nanocrystals: Ligand Exchange Characteristics of a New Binding Motif. *Angew. Chem. Int. Ed.* **2015**, *54*, 6488–6491.
- (43) De Roo, J.; Yazdani, N.; Drijvers, E.; Lauria, A.; Maes, J.; Owen, J. S.; Van Driessche, I.; Niederberger, M.; Wood, V.; Martins, J. C.; et al., Probing Solvent–Ligand Interactions in Colloidal Nanocrystals by the NMR Line Broadening. *Chem. Mater.* **2018**, *30*, 5485–5492.
- (44) Hens, Z. Ligands on Nanocrystal Surfaces, the ^1H Nuclear Magnetic Resonance Fingerprint. *Acc. Chem. Res.* **2023**, *56*, 1623–1633.
- (45) De Roo, J.; Zhou, Z.; Wang, J.; Deblock, L.; Crosby, A. J.; Owen, J. S.; Nonnenmann, S. S. Synthesis of Phosphonic Acid Ligands for Nanocrystal Surface Functionalization and Solution Processed Memristors. *Chem. Mater.* **2018**, *30*, 8034–8039.
- (46) Dhaene, E.; Coppennolle, S.; Deblock, L.; De Buysser, K.; De Roo, J. Binding Affinity of Monoalkyl Phosphinic Acid Ligands toward Nanocrystal Surfaces. *Chem. Mater.* **2023**, *35*, 558–569.
- (47) De Roo, J.; Van Driessche, I.; Martins, J. C.; Hens, Z. Colloidal Metal Oxide Nanocrystal Catalysis by Sustained Chemically Driven Ligand Displacement. *Nat. Mater.* **2016**, *15*, 517–521.
- (48) De Keukeleere, K.; Coucke, S.; De Canck, E.; Van Der Voort, P.; Delpech, F.; Coppel, Y.; Hens, Z.; Van Driessche, I.; Owen, J. S.; De Roo, J. Stabilization of Colloidal Ti, Zr, and Hf Oxide Nanocrystals by Protonated Tri-*n*-octylphosphine Oxide (TOPO) and Its Decomposition Products. *Chem. Mater.* **2017**, *29*, 10233–10242.
- (49) Anderson, N. C.; Chen, P. E.; Buckley, A. K.; De Roo, J.; Owen, J. S. Stereoelectronic

- Effects on the Binding of Neutral Lewis Bases to CdSe Nanocrystals. *J. Am. Chem. Soc.* **2018**, *140*, 7199–7205.
- (50) De Nolf, K.; Cosseddu, S. M.; Jasieniak, J. J.; Drijvers, E.; Martins, J. C.; Infante, I.; Hens, Z. Binding and Packing in Two-Component Colloidal Quantum Dot Ligand Shells: Linear versus Branched Carboxylates. *J. Am. Chem. Soc.* **2017**, *139*, 3456–3464.
- (51) Drijvers, E.; De Roo, J.; Martins, J. C.; Infante, I.; Hens, Z. Ligand Displacement Exposes Binding Site Heterogeneity on CdSe Nanocrystal Surfaces. *Chem. Mater.* **2018**, *30*, 1178–1186.
- (52) Calvin, J. J.; O'Brien, E. A.; Sedlak, A. B.; Balan, A. D.; Alivisatos, A. P. Thermodynamics of Composition Dependent Ligand Exchange on the Surfaces of Colloidal Indium Phosphide Quantum Dots. *ACS Nano* **2021**, *15*, 1407–1420.
- (53) Hens, Z.; De Roo, J. Atomically Precise Nanocrystals. *J. Am. Chem. Soc.* **2020**, *142*, 15627–15637.
- (54) Puchberger, M.; Kogler, F. R.; Jupa, M.; Gross, S.; Fric, H.; Kickelbick, G.; Schubert, U. Can the Clusters $Zr_6O_4(OH)_4(OOCR)_{12}$ and $[Zr_6O_4(OH)_4(OOCR)_{12}]_2$ Be Converted into Each Other? *Eur. J. Inorg. Chem.* **2006**, *2006*, 3283–3293.
- (55) Chen, G.-H.; He, Y.-P.; Zhang, S.-H.; Zhang, L. A series of zirconium-oxo cluster complexes based on arsenate or phosphonate ligands. *Inorg. Chem. Commun.* **2018**, *97*, 125–128.
- (56) Czakler, M.; Schubert, U. Phosphonate-substituted zirconium oxo clusters. *Monatsh. Chem.* **2015**, *146*, 1371–1374.
- (57) Ji, Z.; Zhang, H.; Liu, H.; Yaghi, O. M.; Yang, P. Cytoprotective metal-organic frameworks for anaerobic bacteria. *Proc. Natl. Acad. Sci.* **2018**, *115*, 10582–10587.

- (58) Czakler, M.; Artner, C.; Schubert, U. Influence of the Phosphonate Ligand on the Structure of Phosphonate-Substituted Titanium Oxo Clusters. *Eur. J. Inorg. Chem.* **2013**, *2013*, 5790–5796.
- (59) Guerrero, G.; Mehring, M.; Hubert Mutin, P.; Dahan, F.; Vioux, A. Syntheses and single-crystal structures of novel soluble phosphonato- and phosphinato-bridged titanium oxo alkoxides. *J. Chem. Soc., Dalton Trans.* **1999**, 1537–1538.
- (60) Mehring, M.; Guerrero, G.; Dahan, F.; Mutin, P. H.; Vioux, A. Syntheses, Characterizations, and Single-Crystal X-ray Structures of Soluble Titanium Alkoxide Phosphonates. *Inorg. Chem.* **2000**, *39*, 3325–3332.
- (61) Krämer, T.; Tuna, F.; Pike, S. D. Photo-redox reactivity of titanium-oxo clusters: mechanistic insight into a two-electron intramolecular process, and structural characterisation of mixed-valent Ti(III)/Ti(IV) products. *Chem. Sci.* **2019**, *10*, 6886–6898.
- (62) Russell-Webster, B.; Lopez-Nieto, J.; Abboud, K. A.; Christou, G. Phosphorus-based ligand effects on the structure and radical scavenging ability of molecular nanoparticles of CeO₂. *Dalton Trans.* **2021**, *50*, 15524–15532.
- (63) Xie, H.; Kirlikovali, K. O.; Chen, Z.; Idrees, K. B.; Islamoglu, T.; Farha, O. K. A synthetic strategy towards single crystals of Zr₆ cluster and phosphonate-based metal–organic frameworks. *J. Mater. Chem. A* **2024**, *12*, 6399–6404.
- (64) Hennig, C.; Weiss, S.; Kraus, W.; Kretzschmar, J.; Scheinost, A. C. Solution Species and Crystal Structure of Zr(IV) Acetate. *Inorg. Chem.* **2017**, *56*, 2473–2480.
- (65) Dhaene, E.; Pokratath, R.; Aalling-Frederiksen, O.; Jensen, K. M. O.; Smet, P. F.; De Buysser, K.; De Roo, J. Monoalkyl Phosphinic Acids as Ligands in Nanocrystal Synthesis. *ACS Nano* **2022**, *16*, 7361–7372.

- (66) Kickelbick, G.; Wiede, P.; Schubert, U. Variations in capping the $\text{Zr}_6\text{O}_4(\text{OH})_4$ cluster core: X-ray structure analyses of $[\text{Zr}_6(\text{OH})_4\text{O}_4(\text{OOC}-\text{CH}=\text{CH}_2)_{10}]_2(\mu-\text{OOC}-\text{CH}=\text{CH}_2)_4$ and $\text{Zr}_6(\text{OH})_4\text{O}_4(\text{OOCR})_{12}(\text{PrOH})$ ($\text{R}=\text{Ph}$, $\text{CMe}=\text{CH}_2$). *Inorg. Chim. Acta* **1999**, *284*, 1–7.
- (67) Calcabrini, M.; Van den Eynden, D.; Ribot, S. S.; Pokratath, R.; Llorca, J.; De Roo, J.; Ibáñez, M. Ligand Conversion in Nanocrystal Synthesis: The Oxidation of Alkylamines to Fatty Acids by Nitrate. *JACS Au* **2021**, *1*, 1898–1903.
- (68) Lushtinets, R.; Seifert, G.; Jaehne, E.; Adler, H.-J. P. Infrared Spectra of Alkylphosphonic Acid Bound to Aluminium Surfaces. *Macromol. Symp.* **2007**, *254*, 248–253.
- (69) Gao, W.; Dickinson, L.; Grozinger, C.; Morin, F. G.; Reven, L. Self-Assembled Monolayers of Alkylphosphonic Acids on Metal Oxides. *Langmuir* **1996**, *12*, 6429–6435.
- (70) Dufek, E. J.; Buttry, D. A. Characterization of Zr(IV)–Phosphonate Thin Films Which Inhibit O_2 Reduction on AA2024-T3. *J. Electrochem. Soc.* **2009**, *156*, C322.
- (71) Frey, B. L.; Hanken, D. G.; Corn, R. M. Vibrational spectroscopic studies of the attachment chemistry for zirconium phosphonate multilayers at gold and germanium surfaces. *Langmuir* **1993**, *9*, 1815–1820.
- (72) Hong, H. G.; Sackett, D. D.; Mallouk, T. E. Adsorption of well-ordered zirconium phosphonate multilayer films on high surface area silica. *Chem. Mater.* **1991**, *3*, 521–527.
- (73) Zeng, R.; Fu, X.; Gong, C.; Sui, Y. Synthesis and catalytic application of zirconium-substituted aminoethyl phosphonate. *J. Mater. Sci.* **2006**, *41*, 4771–4776.
- (74) Vivani, R.; Costantino, F.; Taddei, M. *Metal Phosphonate Chemistry: From Synthesis to Applications*; The Royal Society of Chemistry, 2011.

- (75) Boyle, T. J.; Ottley, L. A. M.; Rodriguez, M. A. Structurally characterized carboxylic acid modified zirconium alkoxides for the production of zirconium oxide thin films. *Polyhedron* **2005**, *24*, 1727–1738.
- (76) Kogler, F. R.; Jupa, M.; Puchberger, M.; Schubert, U. Control of the ratio of functional and non-functional ligands in clusters of the type $Zr_6O_4(OH)_4(\text{carboxylate})_{12}$ for their use as building blocks for inorganic–organic hybrid polymers. *J. Mater. Chem.* **2004**, *14*, 3133–3138.
- (77) Kickelbick, G.; Schubert, U. Hydroxy carboxylate substituted oxozirconium clusters. *J. Chem. Soc., Dalton Trans.* **1999**, 1301–1306.
- (78) Nateghi, B.; Boldog, I.; Domasevitch, K. V.; Janiak, C. More versatility than thought: large Zr_{26} oxocarboxylate cluster by corner-sharing of standard octahedral subunits. *CrystEngComm* **2018**, *20*, 5132–5136.
- (79) Poojary, M. D.; Hu, H.-L.; Campbell III, F. L.; Clearfield, A. Determination of crystal structures from limited powder data sets: crystal structure of zirconium phenylphosphonate. *Acta Crystallogr., Sec. B* **1993**, *49*, 996–1001.
- (80) Gomes, R.; Hassinen, A.; Szczygiel, A.; Zhao, Q.; Vantomme, A.; Martins, J. C.; Hens, Z. Binding of Phosphonic Acids to CdSe Quantum Dots: A Solution NMR Study. *J. Phys. Chem. Lett.* **2011**, *2*, 145–152.
- (81) Knauf, R. R.; Lennox, J. C.; Dempsey, J. L. Quantifying Ligand Exchange Reactions at CdSe Nanocrystal Surfaces. *Chem. Mater.* **2016**, *28*, 4762–4770.
- (82) Ritchhart, A.; Cossairt, B. M. Quantifying Ligand Exchange on InP Using an Atomically Precise Cluster Platform. *Inorg. Chem.* **2019**, *58*, 2840–2847.
- (83) Gagnon, K. J.; Perry, H. P.; Clearfield, A. Conventional and Unconventional

- Metal–Organic Frameworks Based on Phosphonate Ligands: MOFs and UMOFs. *Chem. Rev.* **2012**, *112*, 1034–1054, PMID: 22126609.
- (84) Wang, F.; Tang, R.; Buhro, W. E. The Trouble with TOPO; Identification of Adventitious Impurities Beneficial to the Growth of Cadmium Selenide Quantum Dots, Rods, and Wires. *Nano Lett.* **2008**, *8*, 3521–3524, PMID: 18754691.
- (85) Van den Eynden, D.; Unniram Parambil, A. R.; Balog, S.; De Roo, J. Solution Characterization of Zirconium Oxo Clusters. *ChemRxiv* **2024**,
- (86) Kühne, T. D. et al. CP2K: An electronic structure and molecular dynamics software package - Quickstep: Efficient and accurate electronic structure calculations. *J. Chem. Phys.* **2020**, *152*, 194103.
- (87) Perdew, J. P.; Burke, K.; Ernzerhof, M. Generalized Gradient Approximation Made Simple. *Phys. Rev. Lett.* **1996**, *77*, 3865–3868.
- (88) Goedecker, S.; Teter, M.; Hutter, J. Separable dual-space Gaussian pseudopotentials. *Phys. Rev. B* **1996**, *54*, 1703–1710.
- (89) VandeVondele, J.; Hutter, J. Gaussian basis sets for accurate calculations on molecular systems in gas and condensed phases. *J. Chem. Phys.* **2007**, *127*, 114105.
- (90) Genovese, L.; Deutsch, T.; Goedecker, S. Efficient and accurate three-dimensional Poisson solver for surface problems. *J. Chem. Phys.* **2007**, *127*, 054704.
- (91) Dechert, S. xyz2tab. <https://github.com/radi0sus/xyz2tab>, 2016.
- (92) Ashiotis, G.; Deschildre, A.; Nawaz, Z.; Wright, J. P.; Karkoulis, D.; Picca, F. E.; Kieffer, J. The fast azimuthal integration Python library:pyFAI. *J. Appl. Crystallogr.* **2015**, *48*, 510–519.
- (93) Wright CJ, Z. X. Computer-assisted area detector masking. *J. Synchrotron Radiat.* **2017**, *24(Pt 2)*, 506–508.

- (94) Juhas, P.; Davis, T.; Farrow, C. L.; Billinge, S. J. L. PDFgetX3: a rapid and highly automatable program for processing powder diffraction data into total scattering pair distribution functions. *J. Appl. Crystallogr.* **2013**, *46*, 560–566.
- (95) Yang, X.; Juhas, P.; Farrow, C. L.; Billinge, S. J. xPDFsuite: an end-to-end software solution for high throughput pair distribution function transformation, visualization and analysis. *arXiv preprint arXiv:1402.3163* **2014**,
- (96) Juhas, P.; Farrow, C. L.; Yang, X.; Knox, K. R.; Billinge, S. J. L. Complex modeling: a strategy and software program for combining multiple information sources to solve ill posed structure and nanostructure inverse problems. *Acta Crystallogr.* **2015**, 562–568.
- (97) Zobel, M.; Neder, R. B.; Kimber, S. A. J. Universal solvent restructuring induced by colloidal nanoparticles. *Science* **2015**, *347*, 292–294.

TOC Graphic

